

# Variability of stalagmite-inferred Indian monsoon precipitation over the past 252,000 y

Yanjun Cai<sup>a,b,1</sup>, Inez Y. Fung<sup>c,1</sup>, R. Lawrence Edwards<sup>d</sup>, Zhisheng An<sup>a,e</sup>, Hai Cheng<sup>b,d</sup>, Jung-Eun Lee<sup>f</sup>, Liangcheng Tan<sup>a</sup>, Chuan-Chou Shen<sup>g</sup>, Xianfeng Wang<sup>h</sup>, Jesse A. Day<sup>c</sup>, Weijian Zhou<sup>a</sup>, Megan J. Kelly<sup>d</sup>, and John C. H. Chiang<sup>c</sup>

<sup>a</sup>State Key Lab of Loess and Quaternary Geology, Institute of Earth Environment, Chinese Academy of Sciences, Xi'an 710075, China; <sup>b</sup>Institute of Global Environmental Change, Xi'an Jiaotong University, Xi'an 710049, China; <sup>c</sup>Center for Atmospheric Sciences, University of California, Berkeley, CA 94720;

<sup>d</sup>Department of Earth Sciences, University of Minnesota, Minneapolis, MN 55455; <sup>e</sup>Joint Center for Global Change Studies, Beijing 100875, China;

<sup>f</sup>Department of Geological Sciences, Brown University, Providence, RI 02912; <sup>g</sup>High-Precision Mass Spectrometry and Environment Change Laboratory, Department of Geosciences, National Taiwan University, Taipei 106, Taiwan; and <sup>h</sup>Earth Observatory of Singapore, Nanyang Technological University, Singapore 639798

Contributed by Inez Y. Fung, January 14, 2015 (sent for review June 12, 2014; reviewed by Tony Broccoli and Dominique Genty)

A speleothem  $\delta^{18}\text{O}$  record from Xiaobailong cave in southwest China characterizes changes in summer monsoon precipitation in Northeastern India, the Himalayan foothills, Bangladesh, and northern Indochina over the last 252 kyr. This record is dominated by 23-kyr precessional cycles punctuated by prominent millennial-scale oscillations that are synchronous with Heinrich events in the North Atlantic. It also shows clear glacial-interglacial variations that are consistent with marine and other terrestrial proxies but are different from the cave records in East China. Corroborated by isotope-enabled global circulation modeling, we hypothesize that this disparity reflects differing changes in atmospheric circulation and moisture trajectories associated with climate forcing as well as with associated topographic changes during glacial periods, in particular redistribution of air mass above the growing ice sheets and the exposure of the “land bridge” in the Maritime continents in the western equatorial Pacific.

Indian summer monsoon | stalagmite |  $\delta^{18}\text{O}$  | precipitation | glacial-interglacial

The Indian summer monsoon (ISM), a key component of tropical climate, provides vital precipitation to southern Asia. The ISM is characterized by two regions of precipitation maxima: a narrow coastal region along the Western Ghats, denoted by ISM<sub>A</sub>, with moisture from the Arabian Sea, and a broad “Monsoon Zone” around 20°N in northeastern India, denoted by ISM<sub>B</sub>, where storms emanate from the Bay of Bengal and whose rainfall variability is well correlated with that of “All India” rainfall (1). Multiple proxies obtained from Arabian Sea sediments have revealed the variability of summer monsoon winds on timescales of 10<sup>1</sup> to 10<sup>5</sup> y (e.g., refs. 2–6). Our understanding of the paleo-precipitation variability of ISM<sub>B</sub> remains incomplete, owing to the scarcity of long and high-resolution records. Here we present a 252,000-y-long speleothem  $\delta^{18}\text{O}$  record from Xiaobailong cave, southwest China and characterize variability in the ISM<sub>B</sub> precipitation on multiple timescales.

Xiaobailong (XBL, “Little White Dragon”) cave is located in Yunnan Province, southwestern China, near the southeastern edge of the Tibetan Plateau (103°21' E, 24°12' N, ~1,500 m above sea level; *SI Appendix*, Fig. S1). Local climate is characterized by warm/wet summers and cool/dry winters. The mean annual precipitation of ~960 mm (1960–2000) falls mostly from June through September (~80%) (*SI Appendix*, Fig. S2), indicating the summer monsoon rainfall dominates the annual precipitation at the cave site. The temperature in the cave is 17.2 °C, close to local mean annual air temperature (17.3 °C).

Eight stalagmites were collected from the inner chamber (~350 m from the entrance) of the cave, where humidity is ~100% and ventilation is confined to a small crawl-in channel to the outer chamber. One hundred four  $^{230}\text{Th}$  dates were determined on inductively coupled plasma mass spectrometers with typical relative error in age (2 $\sigma$ ) of less than 1% (*Methods* and *SI*

*Appendix*, Table S1 and Figs. S3 and S4). The ages vary monotonically with depth in the stalagmites (*SI Appendix*, Fig. S4) and the  $^{230}\text{Th}$  dates were linearly interpolated to establish chronologies. Measurements of calcite  $\delta^{18}\text{O}$  ( $\delta^{18}\text{O}_c$ ) were made by isotope ratio mass spectrometer on a total of 1,896 samples from the eight stalagmites (*Methods* and *SI Appendix*, Table S2). By matching the chronology established by the absolute  $^{230}\text{Th}$  dates the  $\delta^{18}\text{O}_c$  time series of the different stalagmites were combined to form a single time series. The resulting XBL record (Fig. 1) covers the past 252,000 y, with an average resolution of 70 y between 5.0 and 80.0 thousand years before the present (ka BP, before 1950 AD) and 260 y between 80.0 and 252.0 ka BP, excluding several interruptions of calcite deposition (e.g., during the periods of 52.4–59.8, 164.0–167.2, 204.5–214.1, and 216.8–222.2 ka BP).

In principle, variations in calcite  $\delta^{18}\text{O}_c$  of stalagmites could capture variations of  $\delta^{18}\text{O}$  in precipitation ( $\delta^{18}\text{O}_p$ ), cave temperature, which is close to the surface annual mean temperature, and kinetic loss of CO<sub>2</sub> and evaporation of water during the calcite deposition. We rule out the kinetic fractionation processes, because  $\delta^{18}\text{O}_c$  records from different stalagmites in the XBL cave agree with one another within quoted dating errors over contemporaneous growth periods (Fig. 1), and  $\delta^{13}\text{C}$  records also replicate across speleothems within the cave, suggesting

## Significance

This paper presents a new long speleothem  $\delta^{18}\text{O}$  time series from Xiaobailong cave in southwest China that characterizes changes in a major branch of Indian summer monsoon precipitation over the last 252 kyr. This record shows not only 23-kyr precessional cycles punctuated by prominent millennial-scale weak monsoon events synchronous with Heinrich events in the North Atlantic, but also clear glacial-interglacial variations that are consistent with marine records but different from the cave records in East China. The speleothem records of Xiaobailong and other caves in East China show that the relationship between the Indian and the East Asian summer monsoon precipitation is not invariant, but rather varies on different timescales depending on the nature and magnitude of the climate forcing.

Author contributions: Y.C., I.Y.F., R.L.E., and Z.A. designed research; Y.C., I.Y.F., H.C., J.-E.L., L.T., C.-C.S., and X.W. performed research; Y.C., I.Y.F., R.L.E., Z.A., J.-E.L., J.A.D., W.Z., M.J.K., and J.C.H.C. analyzed data; and Y.C., I.Y.F., R.L.E., Z.A., J.A.D., and J.C.H.C. wrote the paper.

Reviewers: T.B., Rutgers University; and D.G., Laboratoire des Sciences du Climat et de l'Environnement, UMR CEAS/CNRS 1572.

The authors declare no conflict of interest.

<sup>1</sup>To whom correspondence may be addressed. Email: yanjun\_cai@iecas.cn or ifung@berkeley.edu.

This article contains supporting information online at [www.pnas.org/lookup/suppl/doi:10.1073/pnas.1424035112/DCSupplemental](http://www.pnas.org/lookup/suppl/doi:10.1073/pnas.1424035112/DCSupplemental).

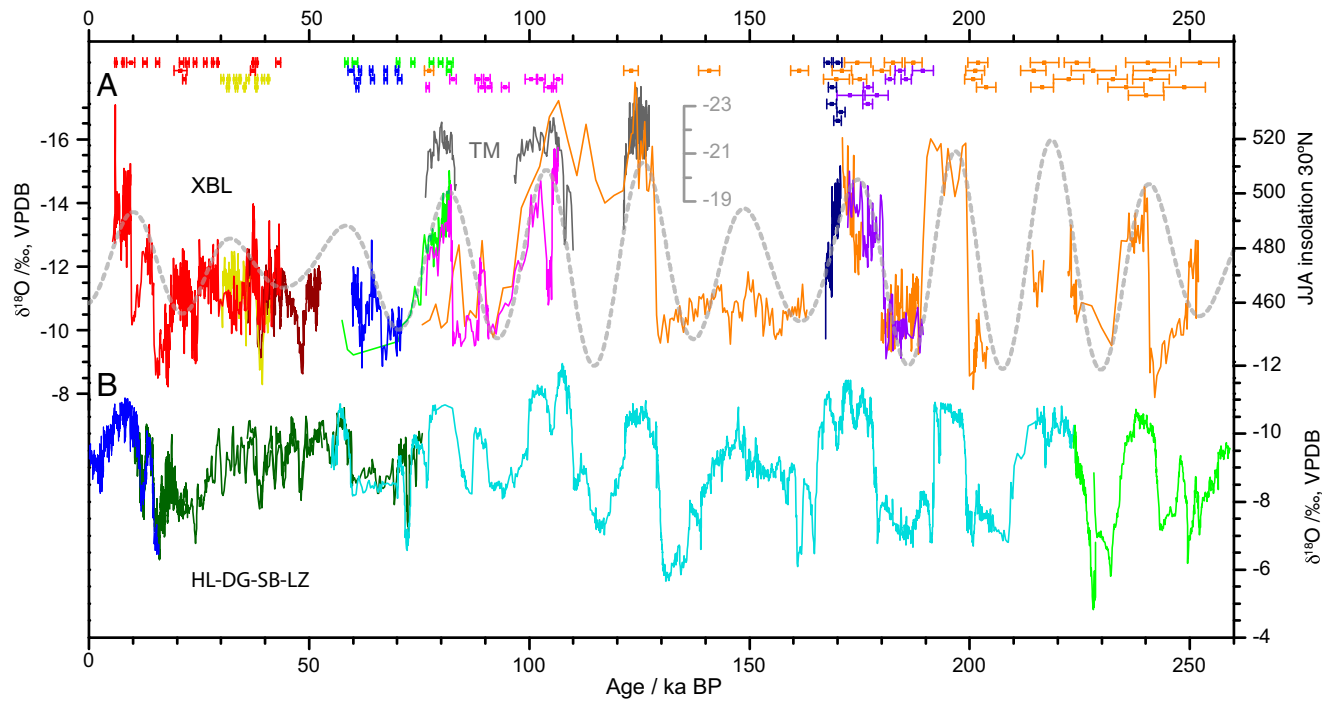


**Fig. 1.** (A) The  $\delta^{18}\text{O}_c$  record of the stalagmites from Xiaobailong cave: XBL-3 (yellow), XBL-4 (green), XBL-7 (blue), XBL-26 (orange), XBL-27 (violet), XBL-29 (red), XBL-48 (pink), XBL-65 (dark blue), and XBL-1 (brown) (12). The gray curve shows a previously established  $\delta^{18}\text{O}_c$  record from the Tibetan Plateau (Tianmen Cave), indicating ISM variations during Marine Isotope Stage 5 (21). The  $^{230}\text{Th}$  dates and errors ( $2\sigma$  error bars) are color-coded by stalagmites. (B) The  $\delta^{18}\text{O}_c$  records of Hulu cave (dark green) (18), Dongge cave (blue) (19), Sanbao cave (sky blue) (20), and Linzhu cave (light green) (20). The  $\delta^{18}\text{O}$  scales for all records shown are reversed (increasing downward). Summer insolation at 30°N (gray dashed line) is integrated over June, July, and August (44).

dominant climate control (*SI Appendix*, Fig. S5). Furthermore, the XBL  $\delta^{18}\text{O}_c$  records broadly resemble, on precessional and millennial timescales for overlapping periods (Fig. 1), speleothem records from Hulu, Dongge, Sanbao, and Linzhu caves (HL-DG-SB-LZ) in East China (7), providing another robust replication test and indicating that the  $\delta^{18}\text{O}_c$  signal in these stalagmites is primarily of climatic origin. The range of calcite  $\delta^{18}\text{O}_c$  change at XBL is  $\sim 8.0\text{‰}$  over 252 kyr. Because temperature-dependent fractionation between calcite and water is likely to be below  $2\text{‰}$  [estimated using  $\sim -0.23\text{‰}/^\circ\text{C}$  (8), and assuming a maximum  $8^\circ\text{C}$  difference between glacial and interglacial periods (9)], the shifts in stalagmite  $\delta^{18}\text{O}_c$  are primarily due to changes in meteoric precipitation  $\delta^{18}\text{O}_{\text{P}}$  at the cave site.

We interpret XBL  $\delta^{18}\text{O}_c$  as an index of  $\text{ISM}_B$  rainfall at a region denoted the Monsoon Zone-B, which encompasses the Monsoon Zone of northeastern India (1), the Himalayan foothills, Bangladesh, and northern Indochina. First, the Bay of Bengal supplies the bulk of moisture to both the Monsoon Zone-B and to XBL across the Indochinese Peninsula, and present-day summer precipitation in the two regions is positively correlated (*SI Appendix*, Fig. S6). Second, multiple climate model simulations show similar 850-hPa wind trajectories for these two regions for both present day and Last Glacial Maximum (LGM), suggesting moisture paths from the Bay of Bengal to XBL were relatively stable in the past (*SI Appendix*, Fig. S7). Third, the XBL  $\delta^{18}\text{O}_c$  record shows good agreement ( $r = 0.56$ ), over the past 100 ka, with the salinity proxy, and by inference fluvial runoff proxy, reconstructed from ODP core 126 KL in the Bay of Bengal (10), with decreased  $\delta^{18}\text{O}_c$  values at XBL corresponding with lower salinity and hence increased precipitation, and vice versa (*SI Appendix*, Fig. S8). We hereafter define a “strong”  $\text{ISM}_B$  as an increase of precipitation over the Monsoon Zone-B, and a corresponding decrease of  $\delta^{18}\text{O}_c$  value at XBL (*SI Appendix*, *SI Materials and Methods*).

## Variability of Indian Summer Monsoon

The dominant variability of XBL  $\delta^{18}\text{O}_c$  aligns well with Northern Hemisphere summer (June–August) insolation (NHSI) variation on a  $\sim 23$ -kyr cycle associated with precession of the Earth’s orbit. Low  $\delta^{18}\text{O}_c$  values, heavier precipitation, or stronger  $\text{ISM}_B$  are associated with higher NHSI, and vice versa. The record is also punctuated by many millennial-scale abrupt events (Fig. 1 and *SI Appendix*, Fig. S8). During the last glacial period (from  $\sim 75$  to  $\sim 20$  ka BP), when the XBL  $\delta^{18}\text{O}_c$  record has a mean resolution as high as  $\sim 70$  y, these abrupt events ( $\sim 15.9$ ,  $\sim 24.3$ ,  $\sim 30.1$ ,  $\sim 39.3$ ,  $\sim 48.2$ , and  $\sim 62.0$  ka BP) are marked by consistent increases of  $\delta^{18}\text{O}_c$ , or weaker  $\text{ISM}_B$ , that are aligned with Heinrich events (11), thus suggesting a link between ISM and climate change in the North Atlantic (4, 12). However, decrease of  $\delta^{18}\text{O}_c$  during apparent warm Dansgaard/Oeschger periods is indistinguishable, likely owing to the resolution of the record.

On glacial–interglacial ( $\sim 100$  kyr) timescales, the XBL calcite  $\delta^{18}\text{O}_c$  values vary between  $\sim -9\text{‰}$  and  $\sim -11\text{‰}$  during glacial periods (e.g., 20–75 ka BP) and are much higher than the  $\sim -14\text{‰}$  of the interglacial optimum periods (e.g., high insolation periods within 75–130 ka BP) (Fig. 1), indicating relatively weak ISM during glacial periods. This is in agreement with other paleomonsoon records (2, 13), especially Chinese loess records that feature a significant glacial–interglacial cycle from 600 ka BP to the present (14).

To separate XBL  $\delta^{18}\text{O}_c$  into its modes of variability, we applied ensemble empirical mode decomposition (EEMD), a new noise-assisted method (15) for analyzing nonlinear, nonstationary time series. Unlike Fourier or wavelet analysis, which decomposes a stationary time series into a chosen set of known functions and seeks each of their global (over the entire time series) amplitudes, EEMD determines, without prior assumptions, instantaneous frequencies and instantaneous amplitudes via a sifting algorithm (15–17). The resulting components are ordered by timescale, from

the shortest to the longest (*SI Appendix*, Fig. S9). For the XBL record, the dominant variability (47.3% of the total variance) is captured by the component C9–10, and shows variability with a  $\delta^{18}\text{O}_c$  range of  $\sim 5\text{\textperthousand}$  that is coincident with NHSI at the precessional timescale ( $\sim 23$  kyr) (Fig. 2). The next component (C11–13) captures 33% of the variance, with a  $\delta^{18}\text{O}_c$  range of  $\sim 4\text{\textperthousand}$ . It peaks around 120 ka and has a broad minimum during the ice ages. Millennial scale variability (C6–8) has a  $\delta^{18}\text{O}_c$  range of  $\sim 4\text{\textperthousand}$  and captures 19% of the variance.

A similar EEMD analysis was applied to the HL-DG-SB-LZ calcite  $\delta^{18}\text{O}_c$  time series from eastern China (7, 18–20) (Fig. 2). The dominant modes of variability at the East China caves are on precessional (69% of variance,  $\delta^{18}\text{O}_c$  range  $\sim 6\text{\textperthousand}$ ) and millennial (19% of the variance,  $\delta^{18}\text{O}_c$  range  $\sim 4\text{\textperthousand}$ ) timescales. Although these modes are similar to those at XBL, on glacial–interglacial timescales the HL-DG-SB-LZ  $\delta^{18}\text{O}_c$  range is only  $\sim 1\text{\textperthousand}$  compared with  $\sim 4\text{\textperthousand}$  at XBL and captures only 11% of the variance.

The correlation coefficient ( $r$ ) between XBL and HL-DG-SB-LZ EEMD components is 0.8 on precessional timescale. The synchrony between the ISM<sub>B</sub> and East Asian Summer Monsoon (EASM), as revealed by EEMD analysis of the long XBL and HL-DG-SB-LZ  $\delta^{18}\text{O}_c$  time series (Figs. 1 and 2), confirms previous observations in intermittent speleothem records from South Asia and East Asia (21–25), thus strengthening the hypothesis that both the Indian and East Asian summer monsoons vary directly in response to changes in NHSI on precessional timescales (7, 26). Our results contradict the hypothesis that winter precipitation affects the phase of EASM cave  $\delta^{18}\text{O}_c$  signals

(27) on precessional timescale, because changes in  $\delta^{18}\text{O}_c$  are synchronous between East China sites and XBL, where the contribution of winter precipitation is negligible. Instead, we point out that the phase of speleothem  $\delta^{18}\text{O}_c$  relative to the insolation signal could vary by up to several thousand years, depending on the choice of reference month(s).

There is no significant correlation ( $r = 0.2$ ) between XBL and HL-DG-SB-LZ  $\delta^{18}\text{O}_c$  on a millennial timescale, even though both show increased  $\delta^{18}\text{O}_c$  values that are synchronous with Heinrich events within quoted errors. Changes in the North Atlantic Ocean during Heinrich events led to circulation changes over the entire Northern Hemisphere (28), and moisture from the Indian Ocean is hypothesized to dominate the isotope composition of precipitation in East Asia (e.g., refs. 28–30). However, two features may preclude attaining a significant correlation on millennial timescales between the two records: First, dating uncertainty in each record may affect the alignment between the two records, especially during the penultimate glacial–interglacial period, and second, several gaps in the XBL record are filled by linear interpolation and do not contain information on millennial timescales. If we correlate the two records at millennial timescales only for the period from 5.4 to 52.4 ka BP where both records are complete and the errors are relatively small, the correlation increases to  $r = 0.46$ , which is significant at the 0.01 level.

### Different Responses of South and East Asian Speleothem $\delta^{18}\text{O}$ on Glacial–Interglacial Timescales

Significant differences exist between the XBL and HL-DG-SB-LZ  $\delta^{18}\text{O}_c$  records. For example, the glacial–interglacial ranges, for example between marine isotope stages (MISs) 5 and 3, in  $\delta^{18}\text{O}_c$  are large and distinct at XBL and barely discernible in the HL-DG-SB-LZ record (Figs. 1 and 2). Furthermore, between MIS 5a and 5c, XBL shows an increasing trend, opposite to that in HL-DG-SB-LZ. The EEMD analysis also shows no significant relationship between XBL and East China speleothem  $\delta^{18}\text{O}_c$  records on the  $\sim 100$ -kyr glacial–interglacial timescale: the correlation coefficient between the two EEMD components is only  $\sim 0.1$ .

To understand the glacial–interglacial differences, we analyze the output of two runs of an isotope-enabled general circulation model with prescribed boundary conditions both for present day and for the LGM (*SI Appendix*, *SI Materials and Methods* and ref. 31). In the model,  $\delta^{18}\text{O}$  of ocean water was specified to be  $0.5\text{\textperthousand}$  for the present day and  $1.7\text{\textperthousand}$  during the LGM because of the loss of water depleted in heavy isotopes to the ice sheets. Relative to present day, LGM summer precipitation decreased substantially over the Indian Ocean and Indian subcontinent, but stratiform precipitation increased over the exposed continental shelf of East Asia (Fig. 3A). Similarly, LGM precipitation  $\delta^{18}\text{O}_p$  was higher, by  $2.0\text{--}4.0\text{\textperthousand}$ , throughout the Indian Ocean and South Asia (including the XBL cave site) but showed either minor increases or decreases of  $1.0\text{--}2.0\text{\textperthousand}$  in East Asia (east of  $105^\circ\text{E}$ ) (Fig. 3B).

To estimate the calcite  $\delta^{18}\text{O}_c$  from the modeled temperature and precipitation  $\delta^{18}\text{O}_p$ , we first used a temperature fractionation of calcite  $\delta^{18}\text{O}_c$  of  $\sim -0.23\text{\textperthousand}/^\circ\text{C}$  and modeled LGM temperature decreases at the cave sites (i.e.,  $\sim 4^\circ\text{C}$  at XBL and  $\sim 6^\circ\text{C}$  at HL-DG-SB-LZ) (*SI Appendix*, Fig. S10), yielding a temperature-based  $\sim 1.0\text{\textperthousand}$  and  $\sim 1.5\text{\textperthousand}$  increase in  $\delta^{18}\text{O}_c$  during the LGM at XBL and at HL-DG-SB-LZ, respectively. The combined temperature and precipitation effect would yield a LGM calcite  $\delta^{18}\text{O}_c$  increase of  $\sim 3.0\text{--}5.0\text{\textperthousand}$  ( $\sim 2.0\text{--}4.0 + 1.0\text{\textperthousand}$ ) at XBL and little change ( $\sim 0.5$  to  $-0.5\text{\textperthousand}$ , or  $-1.0$  to  $-2.0\text{\textperthousand} + 1.5\text{\textperthousand}$ ) at HL-DG-SB-LZ caves. The model results are thus consistent with the observations in speleothem records.

Our model, like other models in the Paleoclimate Modeling Intercomparison Project Phase II suite (9), shows a major

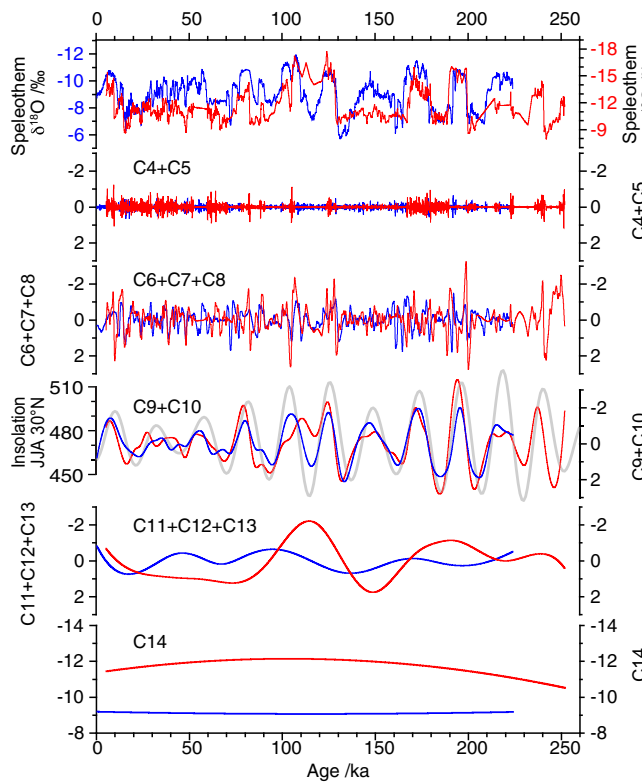


**Fig. 2.** EEMD components of the XBL (red) and Hulu-Dongge-Sanbao (blue) composite time series over the last 252 kyr. During decomposition, noise of 0.4 (0.2 SD of the data) is added for the ensemble calculation, and the ensemble number is 300. Five EEMD components (i.e., sum of components 4–5, sum of components 6–8, sum of components 9–10, sum of components 11–13, and component 14) are presented. Component 14 indicates the overall trend. The individual components are shown in *SI Appendix*, Fig. S9.

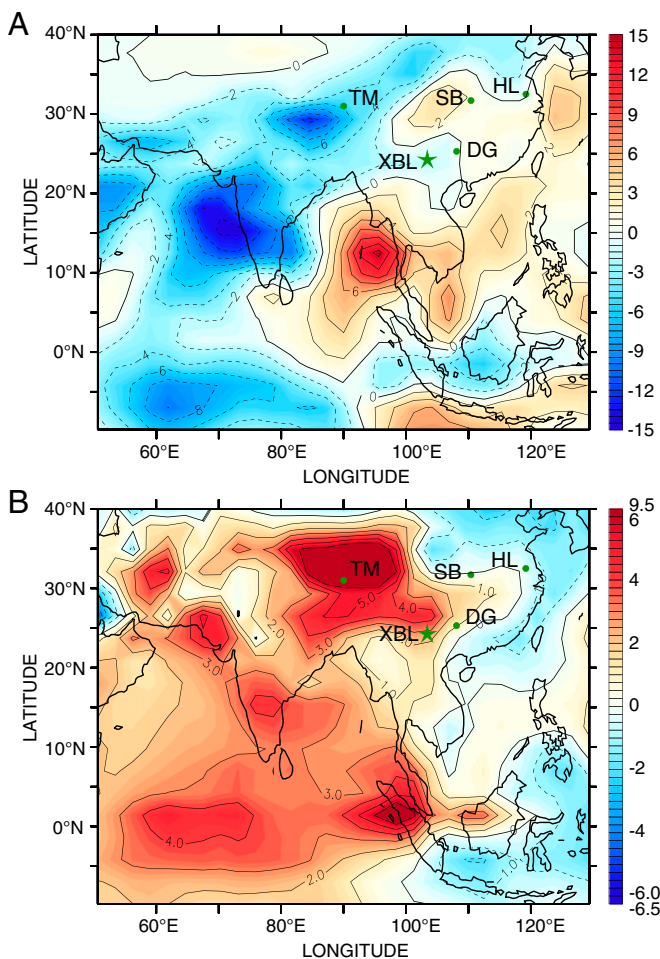


**Fig. 3.** Modeled difference (LGM minus present day) in June–August precipitation (mm/day, A) and amount-weighted precipitation  $\delta^{18}\text{O}_p$  (‰, B). Markers indicate the locations of the following caves: Xiaobailong (XBL), Hulu (HL), Dongge (DG), Sanbao (SB), and Tianmen (TM).

trajectory of moisture advection from the northern reaches of the Bay of Bengal across the Yunnan Plateau and northern Indochina to XBL for the present day and the LGM (Fig. 4). Owing to the lower temperatures during the LGM, there was less moisture transport and precipitation along this path (Figs. 3A and 4). Together with the more enriched source water, LGM vapor  $\delta^{18}\text{O}$  ( $\delta^{18}\text{O}_v$ ) was less depleted (Fig. 4B and C) and  $\delta^{18}\text{O}_p$  was more enriched (+2.0~4.0‰) at XBL.

In contrast, the paths for moisture advection to East China are more varied, with three major paths to the region, a pattern consistent with modern observations\*: from the Arabian Sea across the southern Bay of Bengal (the Indian Ocean path), from the South China Sea and tropical Pacific, and from the North Pacific (Figs. 4 and 5). Atmospheric circulation was different during the LGM, not only because of lower abundance of greenhouse gases, lower sea surface temperatures, and expanded sea ice coverage, but also because of altered topography with elevated continental glaciers and lowered sea level exposing new land surfaces. Off the Pacific coast of Asia, sea level during the LGM was ~120 m lower than today (32), exposing the “land bridge,” the continental shelf around the Gulf of Thailand, South

China Sea, and East China Sea, whereas there were only minor changes around the Bay of Bengal.

During the LGM, the Indian Ocean path of moisture advection to East China was shifted slightly equatorward and strengthened

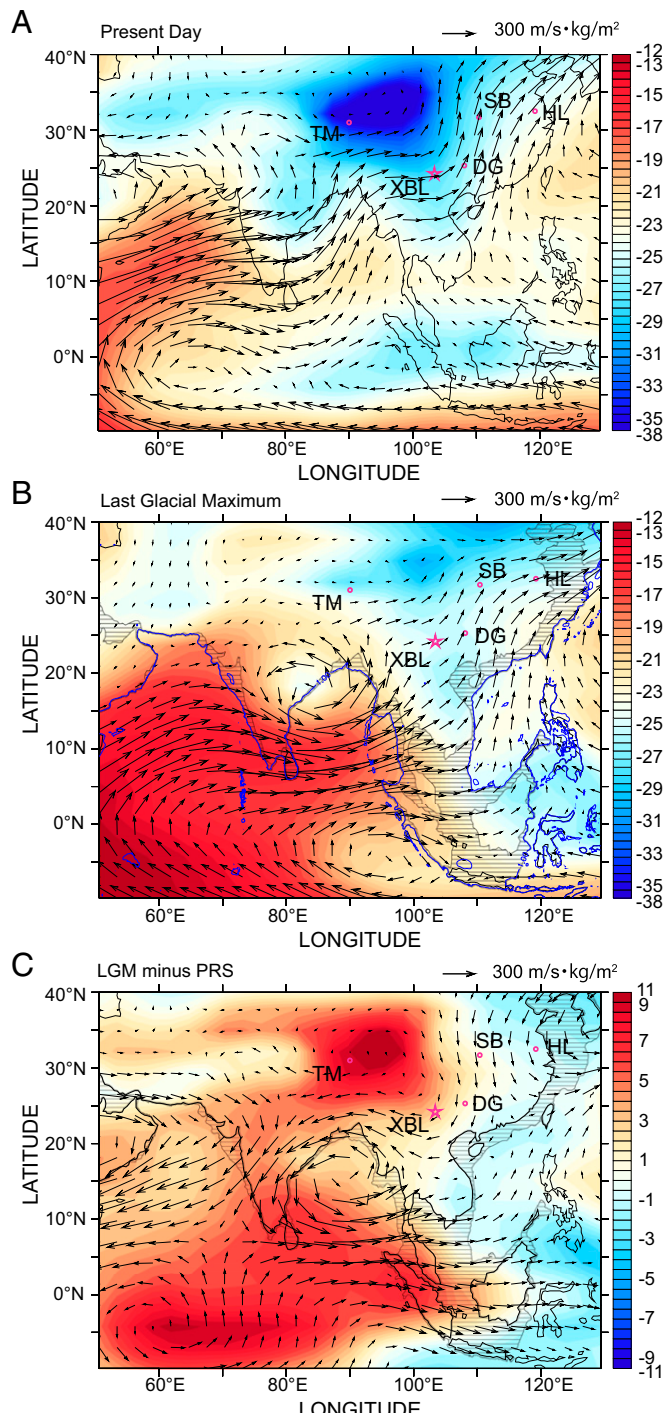


**Fig. 4.** Modeled June–August vapor transport (arrows,  $\text{m s}^{-1} \text{kg}^{-3}$ ) and isotopic composition of column integrated vapor (color-shading, ‰) during the present day (A) and the LGM (B) and the difference between LGM and present day (C). Dark gray lines indicate the present coastline; the blue lines and hatched area in B indicate the coastline and the exposed continental shelf, respectively during the LGM when sea level was ~120 m lower than present day. Markers indicate the locations of the following caves: Xiaobailong (XBL), Hulu (HL), Dongge (DG), Sanbao (SB), and Tianmen (TM).

\*Liu TW, Tang W, Second International Tropical Rainfall Measuring Mission Science Conference, September 6–10, 2004, Tokyo.

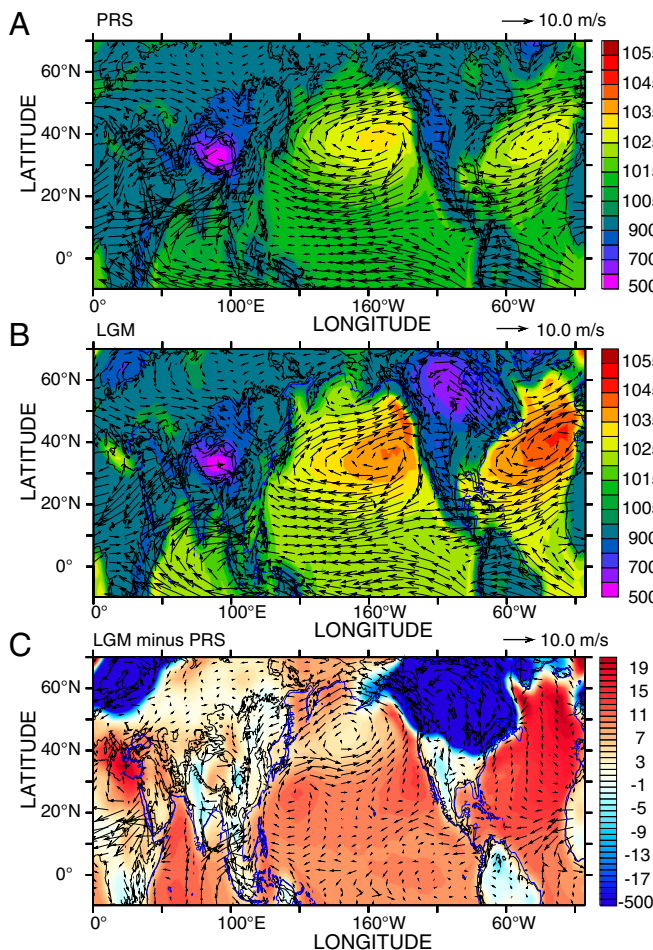


**Fig. 5.** Modeled June–August surface pressure for (A) the present day and (B) the LGM and (C) the departure of LGM surface pressure from the present day (color, hectopascals). The arrows denote the corresponding near-surface winds (averaged over the lowest four layers, ~300 hPa thick, of the model atmosphere). Topography (meters) is contoured. The thick blue line denotes the LGM coastline with a 120-m drop in sea level.

over the southern Bay of Bengal. This path contributed ~30% and 15% of the LGM precipitation at Dongge and Hulu, respectively (28). The trajectory passed over the land bridge, where evaporation was reduced and stratiform precipitation increased relative to the present day (Fig. 3A), contributing to depleted  $\delta^{18}\text{O}_v$  of the vapor (Fig. 4B and C) and lowered  $\delta^{18}\text{O}_p$  values downstream at Dongge, Hulu, and other East China cave sites.

Moisture advection to the Hulu cave region in East China was more complicated during the LGM. Moisture advection from the South China Sea and the tropical Pacific was significantly increased compared with the present day, despite the ~40% decrease in atmospheric water vapor in the LGM atmosphere (7%/K for 6-K decrease) (*SI Appendix*, Fig. S11). This is because southerly and southeasterly winds increased in response to a strengthened east–west pressure gradient between the continent and the Pacific Ocean as well as due to the enhancement of the subtropical high pressure system in the Pacific Ocean (Fig. 5), resulting from the redistribution of air mass from the continents to the oceans as glaciers grew. This increase in moisture flux was countered by an anomalous northeasterly flow from the North Pacific, as a result of greater surface pressure increase over the Bering Sea (~10 hPa) than over the midlatitude ocean (~5 hPa) (Fig. 5). This pattern of pressure difference induced anomalous southeasterly and northeasterly flows toward Eastern China and

together these increased the moisture from the Pacific by ~10% (*SI Appendix*, Fig. S11). As a result of the circulation changes, moisture convergence over the region of the East China caves (110–120E, 20–35N) increased and precipitation increases followed (*SI Appendix*, Fig. S11). In East China, the decrease in  $\delta^{18}\text{O}_v$  from increased precipitation competed with the increase in  $\delta^{18}\text{O}$  of the ocean source, resulting in little change in  $\delta^{18}\text{O}_p$  at HL-DG-SB-LZ.

Taken all together, the circulation changes together with more enriched ocean water result in an unchanged and/or slightly depleted  $\delta^{18}\text{O}_p$  over East China during the LGM, consistent with the observations at cave sites in East China during glacial periods.

### Concluding Remarks

The XBL  $\delta^{18}\text{O}_c$  record documents the variability of the ISM<sub>B</sub> precipitation on glacial–interglacial, precessional, and millennial timescales over the last 252,000 y. Unlike speleothem records from East China, XBL is concordant with records of the ISM<sub>B</sub> from marine sediments and loess records on a glacial–interglacial timescale.

Our modeling results show that glacial–interglacial changes in atmospheric circulation and rainfall are manifested in isotopically different ways at XBL and in East China, with more depleted precipitation  $\delta^{18}\text{O}_p$  during interglacial than during glacial periods at XBL versus nearly unchanged precipitation  $\delta^{18}\text{O}_p$  in East China. We further suggest that reduced evaporation over exposed continental shelf during the LGM could have contributed to the depleted precipitation  $\delta^{18}\text{O}_p$  downstream at some of the cave sites in East China.

Our study, along with other paleoclimate modeling studies, puts forth pieces of the puzzle of how regional circulation and hydrology respond to different climate forcings or perturbations. The model results taken all together show that variations in  $\delta^{18}\text{O}_p$  and, by inference,  $\delta^{18}\text{O}_c$  of speleothems, reflect regional and hemispheric scale variations in vapor flux as well as in situ condensation and evaporation in the atmospheric column (33–36).

The Indian Ocean moisture path to East Asia seems robust, even though the magnitudes of the fluxes vary, in the comparison of the present day and the LGM here and in a comparison of the LGM with or without the Heinrich perturbation (28). In this study, changes in the tropical and North Pacific moisture fluxes dominated the  $\delta^{18}\text{O}_p$  changes in East China during the LGM. Our result that the land bridge exposed during the LGM led to enhanced summer large-scale stratiform precipitation is not inconsistent with the reduction in annual mean convection over the Sunda Shelf (e.g., ref. 34). Although the complexity of circulation changes in influencing precipitation changes of a site or a region is not a surprise, the long speleothem records, such as the XBL  $\delta^{18}\text{O}_c$  data presented here, present unique opportunities for improving climate models and for testing hypotheses about past hydroclimate changes.

### Methods

**U-Series Dating and Stable Isotope Analysis.** All stalagmites were cut into halves along the growth axis and their surfaces were polished. *SI Appendix*, Fig. S3 illustrates images of the stalagmites and the  $^{230}\text{Th}$  dating positions. Subsamples were drilled along growth axes for  $^{230}\text{Th}$  dating at the Minnesota Isotope Laboratory on the inductively coupled plasma mass spectrometers (Thermo-Finnigan ELEMENT and Thermo Fisher NEPTUNE, refs. 37 and 38, respectively). The chemical procedures used to separate the uranium and thorium for  $^{230}\text{Th}$  dating are similar to those described in ref. 39.

Subsamples for stable isotope analysis were collected in two ways: (i) drilling with a dental drill bit 0.5 mm in diameter directly from the polished half of the stalagmite at an average interval of 2, 1, or 0.5 mm along stalagmite axes, depending on sample growth rates, and (ii) cutting the stalagmite into a 1 × 0.5-cm slab using a diamond saw and then scraping off perpendicularly to the growth axes of the stalagmites at a mean resolution of ~20 subsamples per millimeter. The second method was applied for sections between 0 and 95 mm from the top of stalagmite XBL-29. We

performed the stable isotopic analysis on all subsamples collected through the first method and every 10th sample from the second method. A total of 1,896 oxygen isotopic values were obtained on a Finnigan MAT-252 mass spectrometer equipped with Kiel Carbonate Device III at the Institute of Earth Environment, Chinese Academy of Sciences. International standard NBS19 and interlaboratory standard TTB1 were run for every 10–15 samples and arbitrarily selected duplicate measurements were conducted every 10–20 samples, respectively, to check for homogeneity and reproducibility. All oxygen isotopic values are reported in  $\delta$  notation, the per mil deviation relative to the Vienna Pee Dee Belemnite (VPDB) standard ( $\delta^{18}\text{O} = [({^{18}\text{O}}/{^{16}\text{O}})_{\text{sample}}/({^{18}\text{O}}/{^{16}\text{O}})_{\text{standard}} - 1] \times 1000$ ). Standard results show that the precision of  $\delta^{18}\text{O}_{\text{C}}$  analysis is better than 0.15‰ (2 $\sigma$ ).

**Isotope-Enabled General Circulation Model Simulations.** The climate model used in this project incorporated HDO and  $\text{H}_2^{18}\text{O}$  into the NCAR CAM2. We then ran this isotope-enabled model with fixed sea surface temperature (SST) and sea ice distributions for the present day and the LGM (40). SST in the present-day run is given by the climatological monthly mean derived from observations from 1949 to 2001. In the LGM run, we used monthly SST

and sea ice distribution simulated by the fully coupled atmosphere–land–ocean–ice Community Climate System Model (41) with atmospheric carbon dioxide ( $\text{CO}_2$ ), methane ( $\text{CH}_4$ ), and nitrous oxide ( $\text{N}_2\text{O}$ ) at 185 ppmv, 350 ppbv, and 200 ppbv, respectively. The LGM ICE-5G reconstruction is used for the continental ice sheet extent and topography prescription. Surface ocean  $\delta^{18}\text{O}$  values for the present day and LGM are prescribed as 0.5‰ (42) and 1.7‰ (43), respectively. The isotope-CAM LGM simulation is initialized using the atmospheric state from the equilibrium simulation of the CCSM LGM run and is integrated forward for 20 y using SSTs and glacial and sea ice extents from CCSM as boundary conditions. The present-day simulation was integrated for 15 y. In both cases, averages of the last 10 y were used for the analysis.

**ACKNOWLEDGMENTS.** We thank Prof. P. Molnar and the reviewers for valuable suggestions. This work was supported by National Natural Science Foundation of China grants; National Basic Research Program of China; the Knowledge Innovation Program of the Chinese Academy of Sciences; National Science Foundation Grants EAR-0909195 and EAR-1211925 (to I.Y.F.) and EAR-0908792 and EAR-1211299 (to R.L.E. and H.C.); Taiwan Ministry of Science and Technology Grant MOST-103-2119-M-002-022 (to C.-C.S.); and a Singapore National Research Foundation fellowship.

1. Gadgil S (2003) The Indian monsoon and its variability. *Annu Rev Earth Planet Sci* 31: 429–467.
2. Prell WL, Kutzbach JE (1987) Monsoon variability over the past 150,000 years. *J Geophys Res* 92:8411–8425.
3. Sirocko F, et al. (1993) Century-scale events in monsoonal climate over the past 24,000 years. *Nature* 364:322–324.
4. Schulz H, Rad UV, Erlenkeuser H (1998) Correlation between Arabian Sea and Greenland climate oscillations of the past 110,000 years. *Nature* 393:54–57.
5. Clemens SC, Prell WL (2003) A 350,000 year summer-monsoon multi-proxy stack from the Owen Ridge, Northern Arabian Sea. *Mar Geol* 201:35–51.
6. Gupta AK, Anderson DM, Overpeck JT (2003) Abrupt changes in the Asian southwest monsoon during the Holocene and their links to the North Atlantic Ocean. *Nature* 421(6921):354–357.
7. Wang Y, et al. (2008) Millennial- and orbital-scale changes in the East Asian monsoon over the past 224,000 years. *Nature* 451(7182):1090–1093.
8. Kim ST, O’Neil JR (1997) Equilibrium and nonequilibrium oxygen isotope effects in synthetic carbonates. *Geochim Cosmochim Acta* 61:3461–3475.
9. Braconnot P, et al. (2007) Results of PMIP2 coupled simulations of the Mid-Holocene and Last Glacial Maximum – Part 1: Experiments and large-scale features. *Clim Past* 3: 261–277.
10. Kudrass HR, Hofmann A, Doose H, Emeis K, Erlenkeuser H (2001) Modulation and amplification of climatic changes in the Northern Hemisphere by the Indian summer monsoon during the past 80 k.y. *Geology* 29:63–66.
11. Heinrich H (1988) Origin and consequences of cyclic ice rafting in the Northeast Atlantic Ocean during the past 130,000 years. *Quat Res* 29:142–152.
12. Cai YJ, et al. (2006) High-resolution absolute-dated Indian Monsoon record between 53 and 36 ka from Xiaobailong Cave, southwestern China. *Geology* 34:621–624.
13. An Z, et al. (2011) Glacial-interglacial Indian summer monsoon dynamics. *Science* 333(6043):719–723.
14. Lu H, Zhang F, Liu X, Duce RA (2004) Periodicities of palaeoclimatic variations recorded by loess-paleosol sequences in China. *Quat Sci Rev* 23:1891–1900.
15. Wu Z, Huang NE (2009) Ensemble Empirical Mode Decomposition: A noise-assisted data analysis method. *Adv Adapt Data Anal* 1:1–41.
16. Wu Z, Huang NE, Long SR, Peng C-K (2007) On the trend, detrending, and variability of nonlinear and nonstationary time series. *Proc Natl Acad Sci USA* 104(38):14889–14894.
17. Wu Z, Huang NE, Wallace JM, Smoliak BV, Chen X (2011) On the time-varying trend in global-mean surface temperature. *Clim Dyn* 37:759–773.
18. Wang YJ, et al. (2001) A high-resolution absolute-dated late Pleistocene Monsoon record from Hulu Cave, China. *Science* 294(5550):2345–2348.
19. Dykoski CA, et al. (2005) A high-resolution, absolute-dated Holocene and deglacial Asian monsoon record from Dongge Cave, China. *Earth Planet Sci Lett* 233:71–86.
20. Cheng H, et al. (2009) Ice age terminations. *Science* 326(5950):248–252.
21. Cai YJ, et al. (2010) Large variations of oxygen isotopes in precipitation over south-central Tibet during Marine Isotope Stage 5. *Geology* 38:243–246.
22. Fleitmann D, et al. (2007) Holocene ITCZ and Indian monsoon dynamics recorded in stalagmites from Oman and Yemen (Socotra). *Quat Sci Rev* 26:170–188.
23. Sinha A, et al. (2005) Variability of Southwest Indian summer monsoon precipitation during the Bølling–Allerød. *Geology* 33:813–816.
24. Cai YJ, et al. (2012) The Holocene Indian monsoon variability over the southern Tibetan Plateau and its teleconnections. *Earth Planet Sci Lett* 335/336:135–144.
25. Cheng H, Sinha A, Wang X, Cruz F, Edwards R (2012) The Global Paleomonsoon as seen through speleothem records from Asia and the Americas. *Clim Dyn* 39:1045–1062.
26. Kutzbach JE (1981) Monsoon climate of the Early Holocene: Climate experiment with the Earth’s orbital parameters for 9000 years ago. *Science* 214(4516):59–61.
27. Clemens SC, Prell WL, Sun Y (2010) Orbital-scale timing and mechanisms driving Late Pleistocene Indo-Asian summer monsoons: Reinterpreting cave speleothem  $\delta^{18}\text{O}$ . *Paleoceanography* 25(4):PA4207.
28. Pausata FSR, Battisti DS, Nisancioglu KH, Bitz CM (2011) Chinese stalagmite  $\delta^{18}\text{O}$  controlled by changes in the Indian monsoon during a simulated Heinrich event. *Nat Geosci* 4:474–480.
29. Maher BA (2008) Holocene variability of the East Asian summer monsoon from Chinese cave records: A re-assessment. *Holocene* 18:861–866.
30. Dayem KE, Molnar P, Battisti DS, Roe GH (2010) Lessons learned from oxygen isotopes in modern precipitation applied to interpretation of speleothem records of paleoclimate from eastern Asia. *Earth Planet Sci Lett* 295:219–230.
31. Lee JE, Fung I, DePaolo DJ, Henning CC (2007) Analysis of the global distribution of water isotopes using the NCAR atmospheric general circulation model. *J Geophys Res* 112:D16306.
32. Peltier WR (2004) Global glacial isostasy and the surface of the ice-age Earth: The ICE-5G (VM2) model and GRACE. *Annu Rev Earth Planet Sci* 32:111–149.
33. LeGrande AN, Schmidt GA (2009) Sources of Holocene variability of oxygen isotopes in paleoclimate archives. *Clim Past* 5:441–455.
34. DiNezio PN, et al. (2011) The response of the Walker circulation to Last Glacial Maximum forcing: Implications for detection in proxies. *Paleoceanography* 26(3):PA3217.
35. Lee JE, et al. (2012) Asian monsoon hydroclimatology from TES and SCIMACHY water vapor isotope measurement and LMDZ simulations: Implications for speleothem climate record interpretation. *J Geophys Res* 117:D15112.
36. Battisti DS, Ding Q, Roe GH (2014) Coherent pan-Asian climate and isotopic response to orbital forcing of tropical insolation. *J Geophys Res Atmos* 119:11997–12020.
37. Shen C-C, et al. (2002) Uranium and thorium isotopic and concentration measurements by magnetic sector inductively coupled plasma mass spectrometry. *Chem Geol* 185:165–178.
38. Cheng H, et al. (2013) Improvements in  $^{230}\text{Th}$  dating,  $^{230}\text{Th}$  and  $^{234}\text{U}$  half-life values, and U–Th isotopic measurements by multi-collector inductively coupled plasma mass spectrometry. *Earth Planet Sci Lett* 371:82–91.
39. Edwards RL, Chen JH, Wasserburg GJ (1987)  $^{238}\text{U}$ – $^{234}\text{U}$ – $^{230}\text{Th}$  systematic and the precise measurement of time over the past 500,000 years. *Earth Planet Sci Lett* 81: 175–192.
40. Lee JE, Fung I, DePaolo DJ, Otto-Bliesner B (2008) Water isotopes during the Last Glacial Maximum: New general circulation model calculations. *J Geophys Res* 113:D19109.
41. Otto-Bliesner BL, et al. (2006) Last Glacial Maximum and Holocene climate in CCSM3. *J Clim* 19:2526–2544.
42. Hoffmann G, Werner M, Heumann M (1998) Water isotope module of the ECHAM atmospheric general circulation model: A study on timescales from days to several years. *J Geophys Res* 103:16871–16896.
43. Schrag DP, Hampt G, Murray DW (1996) Pore fluid constraints on the temperature and oxygen isotopic composition of the glacial ocean. *Science* 272(5270):1930–1932.
44. Berger A, Loutre MF (1991) Insolation values for the climate of the last 10 million years. *Quat Sci Rev* 10:297–317.

## **Supporting Information Appendix**

### **Variability of stalagmite-inferred Indian Monsoon precipitation over the past 252,000 years**

By Yanjun Cai et al.

### **Table of Contents**

SI Materials and Methods .....	2
Figure S1 .....	4
Figure S2 .....	5
Figure S3 .....	6
Figure S4 .....	7
Figure S5 .....	8
Figure S6 .....	9
Figure S7-a .....	10
Figure S7-b .....	11
Figure S8 .....	12
Figure S9 .....	13
Figure S10 .....	14
Figure S11 .....	15
References .....	16
Table S1 .....	18
Table S2 .....	21

## SI Materials and Methods

**The interpretation of XBL  $\delta^{18}\text{O}_c$ .** As explained in the main text, the amplitude of  $\delta^{18}\text{O}_c$  variations in the XBL speleothem implies a signal dominated by changes in precipitation  $\delta^{18}\text{O}_p$ , rather than a temperature effect alone. Each measurement of precipitation  $\delta^{18}\text{O}_p$  therefore reflects the cumulative history of precipitation and evaporation of water vapor en route to our site. Our interpretation can be simplified through the lens of Rayleigh distillation (1). If we consider an idealized parcel of water vapor that flows from the Bay of Bengal to XBL without any environmental mixing, the  $\delta^{18}\text{O}_v$  of the vapor should become isotopically depleted as a parcel rains out. In practice, Rayleigh distillation cannot be applied in regions with local recycling of vapor during transport or other fractionation processes such as the re-evaporation of raindrops, but the relatively dry terrain of the Yunnan Plateau and Northern Indochina Peninsula should be suitable for such an interpretation.

It is crucial to our proposed interpretation of the XBL record that the path from the Bay of Bengal to our site remains mostly fixed during LGM conditions, and that there are not significant changes in land cover en route. Model results show that the moisture source and transport route remained largely unchanged during the LGM (SI Appendix, Fig. S7; Fig. 4), and sea-land changes around the Bay of Bengal are minor, unlike the exposure of the Sunda Shelf to the southeast.

In an ideal scenario, another speleothem  $\delta^{18}\text{O}_c$  record would be available upstream of XBL, in which case the difference in  $\delta^{18}\text{O}_c$  between the two sites would reflect total rainout amount en route (2, 3). However, it is known that downwind  $\delta^{18}\text{O}_c$  records amplify the variability of changes upstream, a relation observed between the high-altitude Tibetan Plateau and low-altitude Indian Monsoon region in the Holocene (3). As a result, the rainout quantity revealed by subtracting two  $\delta^{18}\text{O}_c$  records should also be independently reflected in each of the individual records. Since precipitation over the Bay of Bengal should account for most precipitation en route, we argue that XBL  $\delta^{18}\text{O}_c$  functions as an index of rainfall over the Bay of Bengal. The good agreement ( $r=0.56$ ) of salinity record KL 126 from the northern Bay of Bengal (4) with XBL provides additional confirmation of this interpretation. We also observe good correlation in rain gauge data between June-July-August precipitation at XBL and precipitation over the Monsoon Region of India. We therefore conclude that XBL  $\delta^{18}\text{O}_c$  serves as a proxy of Indian Monsoon strength, defined as the intensity of rainfall over both the Bay of Bengal and the Monsoon Zone.

**The reliability of our isotope-enabled GCM simulations.** The model used in this paper is the National Center for Atmospheric Research (NCAR) Community Atmospheric Model version 2 (CAM2)(5), into which we have added a water-isotope module (6). The resolution of the atmospheric component of CAM2 is T42 (approximately  $2.8^\circ$  latitude x  $2.8^\circ$  longitude), with 26 vertical atmospheric layers from the surface up to 2 hPa. The water isotope module estimates fractionation associated with evaporation from the surface and in-situ evaporation and

condensation associated with cloud processes. A unique feature is the treatment of temperature- and drop-size dependent isotopic disequilibrium between vapor and raindrops. For the present-day run, the model was forced by climatological monthly mean sea surface temperatures derived from observations from 1949-2001. For the LGM run, continental ice sheet extent and topography was prescribed from the ICE-5G reconstruction (7), and atmospheric CO<sub>2</sub>, CH<sub>4</sub> and N<sub>2</sub>O concentrations of 185ppm, 350 ppb, and 220 ppb respectively were specified. Monthly SST and sea ice distributions were taken from a fully coupled Community Climate System Model (8).

The model is very similar to CAM3 employed in (9) and (10). The limitations of the atmospheric model and isotopic scheme are described by (6). Our LGM and present-day runs have also been previously used to interpret ice core data (11) and precipitation  $\delta^{18}\text{O}_p$  changes in South America (12). As is expected of a relatively coarse-resolution generation circulation model, the modeled present-day precipitation and  $\delta^{18}\text{O}_p$  show biases relative to observations in the vicinity of the Tibetan Plateau. Similar to (9), our model yields reasonable simulations of large-scale circulation changes and can be used to interpret changes over East Asia.

## Supplementary Figures

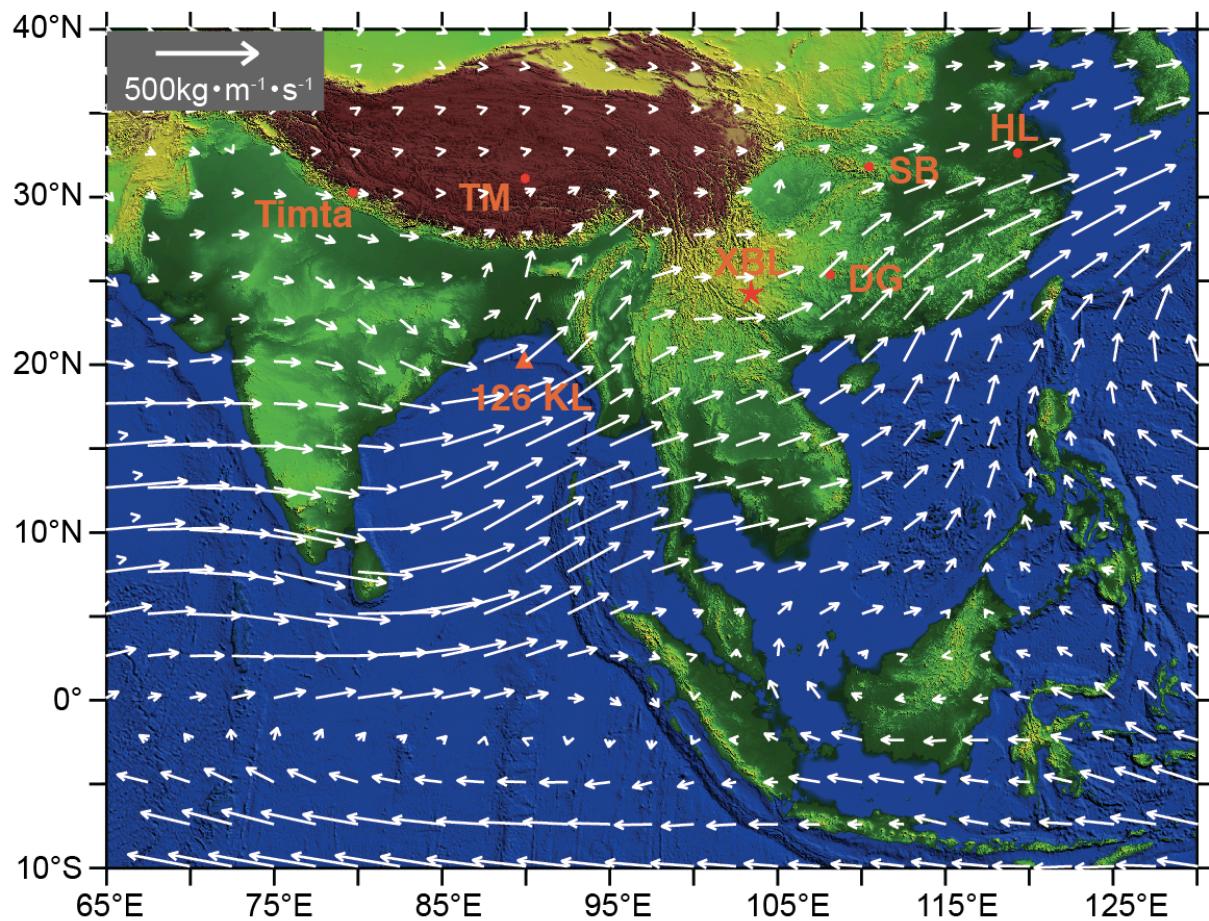


Figure S1. The location of Xiaobailong cave (XBL, red star,  $24^{\circ}12'N$ ,  $103^{\circ}21'E$ ) and present-day moisture transport patterns after the onset of monsoon ( $5^{th}$  pentad of May –  $2^{nd}$  pentad of July, averaged from 1990-1999, adapted from (13)). The locations of other cave sites are indicated by red solid circles: Hulu cave (HL)(14); Dongge cave (DG) (15,16); Sanbao and Linzhu Caves (SB)(17, 18); Tianmen cave (TM) (3, 19) in China; and Timta cave in India (20). The red triangle indicates the location of marine core 126KL (4).

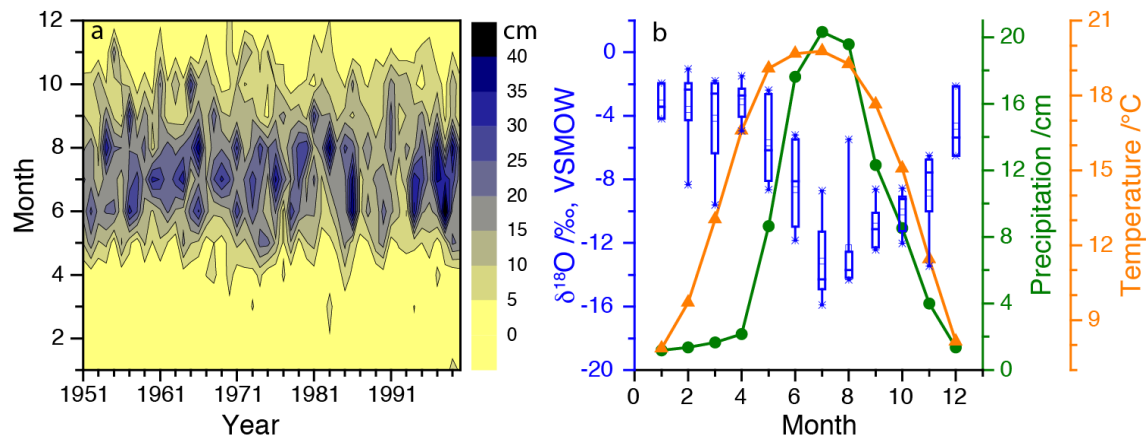


Figure S2. (a) Monthly precipitation for 1951-2000 observed at Kunming meteorological observatory, demonstrating that rainfall is concentrated between June and September. (b) Monthly mean precipitation (green solid circles), temperature (yellow triangles) and  $\delta^{18}\text{O}$  of precipitation (blue box-and-whisker diagram) at Kunming ( $25^{\circ}1' \text{N}$ ,  $102^{\circ}24' \text{E}$ ) meteorological observatory. The  $\delta^{18}\text{O}_p$  data are from the IAEA/WMO 2006 (<http://isohis.iaea.org>).

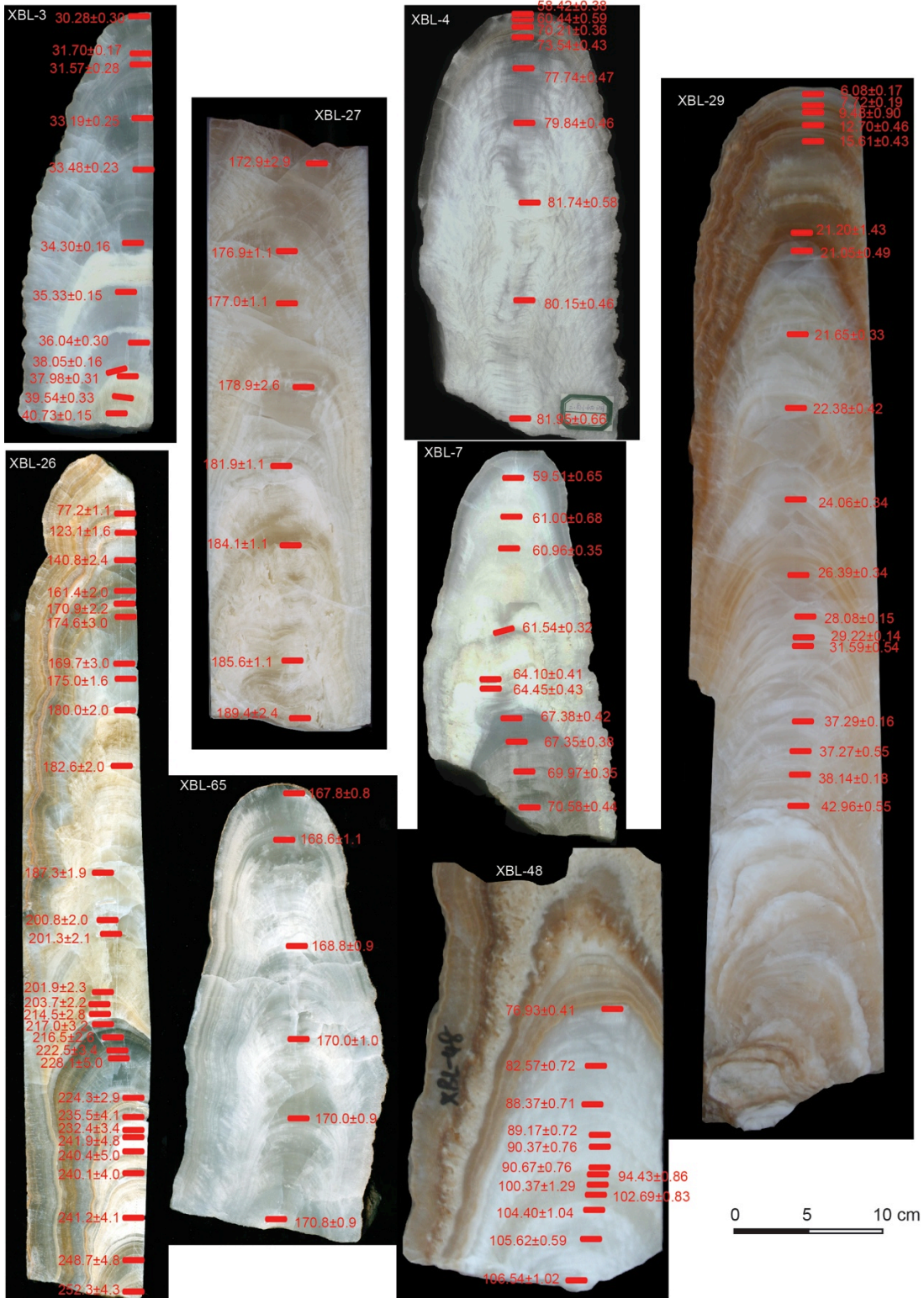


Figure S3. Images of stalagmites used to establish the XBL  $\delta^{18}\text{O}_c$  record. All  $^{230}\text{Th}$  dating positions are marked on the stalagmites with red rectangles, and ages (ka BP) are also labeled with  $2\sigma$  error.

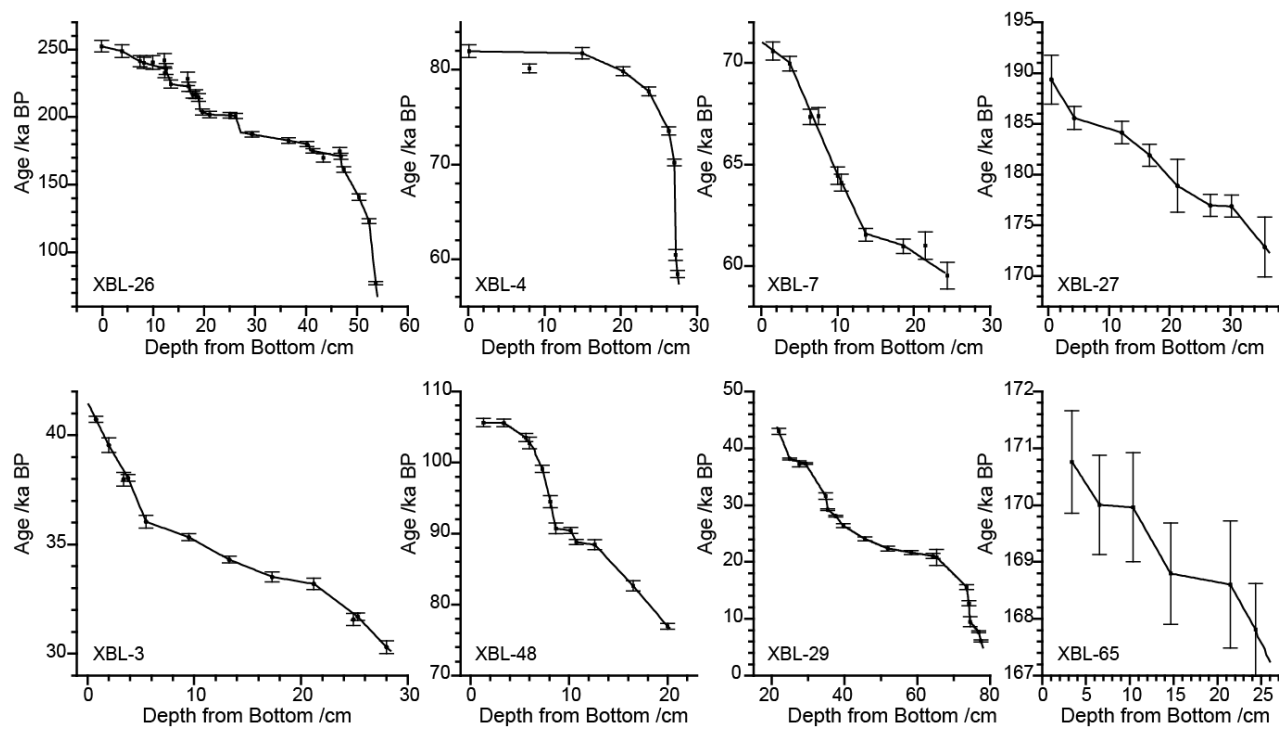


Figure S4. Plots of age versus depth for stalagmites XBL-3, XBL-4, XBL-7, XBL-26, XBL-27, XBL-29, XBL-48 and XBL-65 from Xiaobailong cave. All ages are reported in units of thousands of years before present (1950 AD), ka BP. The age errors indicated in the plots are  $2\sigma$  error. Linear interpolation is used to establish the chronology for each sample.

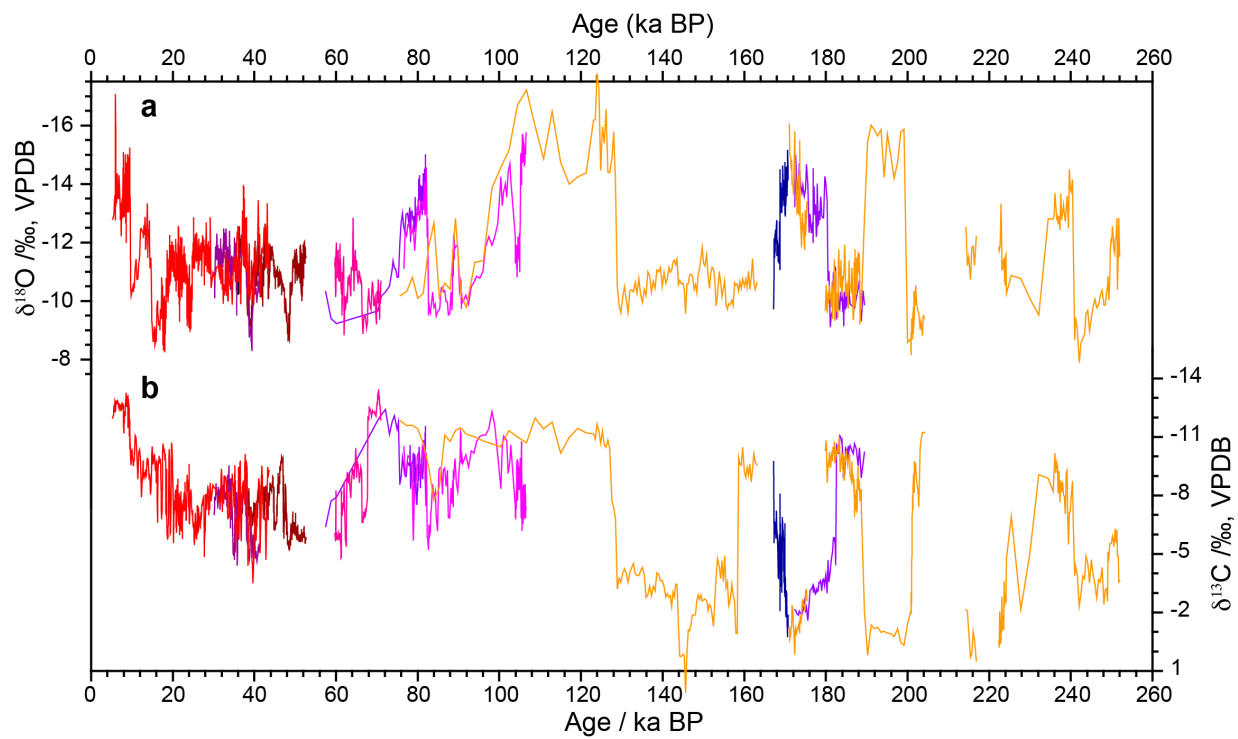


Figure S5. The time series of speleothem  $\delta^{18}\text{O}_c$  and  $\delta^{13}\text{C}$  obtained from Xiaobailong Cave. The different colors denote different stalagmites (the same as in Fig. 1). Replications in both  $\delta^{18}\text{O}_c$  and  $\delta^{13}\text{C}$  profiles indicate that the variations of  $\delta^{18}\text{O}_c$  are dominated by climate variations, i.e., changes in the oxygen isotopic composition of meteoric precipitation and cave temperature at the time of calcite precipitation.

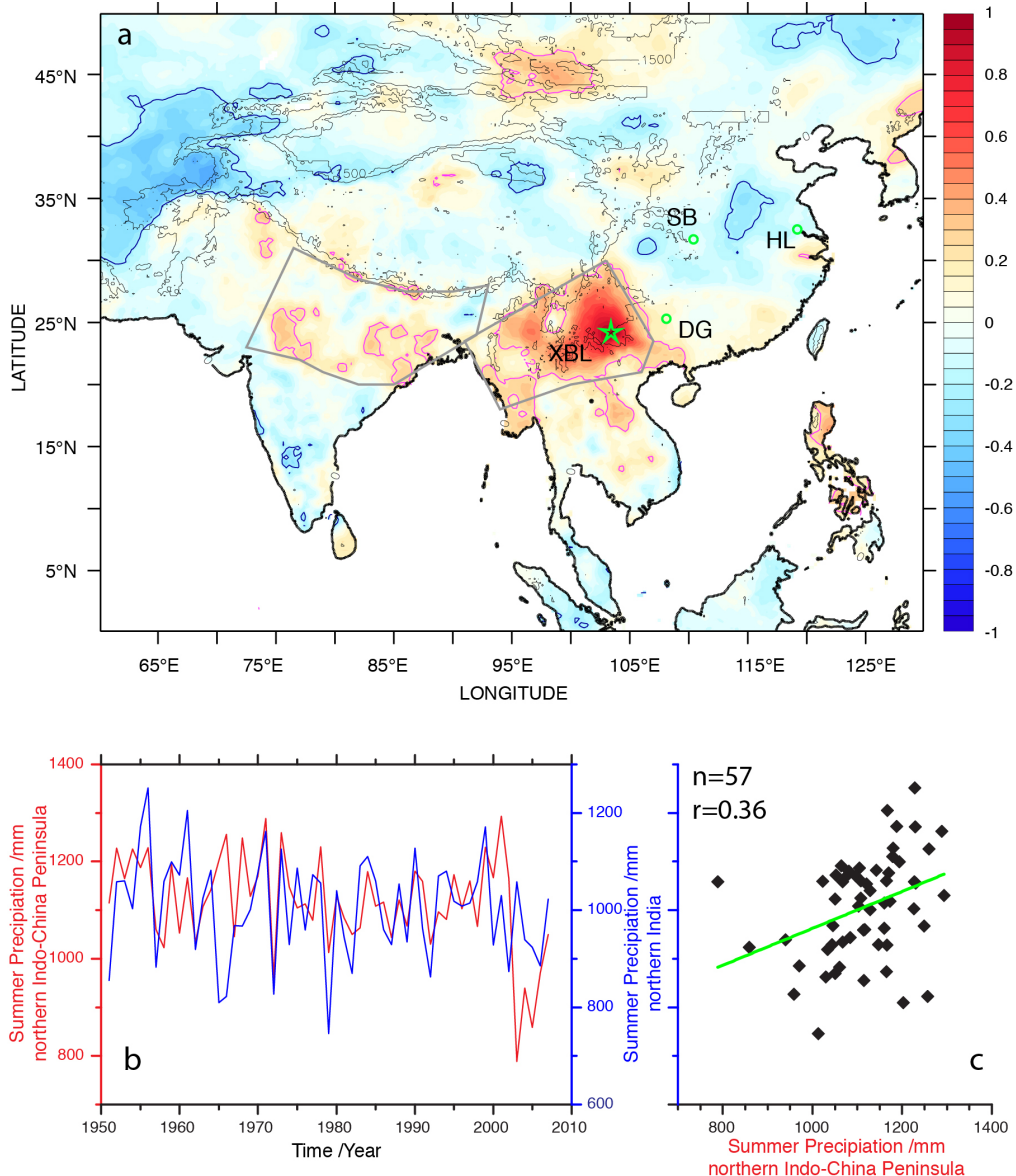


Figure S6. (a) Correlation between summer half-year (May to October) precipitation at XBL cave site and other regions during the period 1951-2007. The pink (blue) contour denotes the region of positive (negative) correlation above 95% confidence level. (b) Comparison of summer half-year average precipitation at northern India and northern Indo-China Peninsula (as denoted by gray polygons in panel a) from 1951-2007. (c) Precipitation of northern India versus that of northern Indo-China Peninsula, indicating the precipitations at these two regions are positively correlated. Data source: APHRODITE (Asian Precipitation - Highly-Resolved Observational Data Integration Towards Evaluation of Water Resources, APHRO\_MA\_V1101R2 product, (21)).

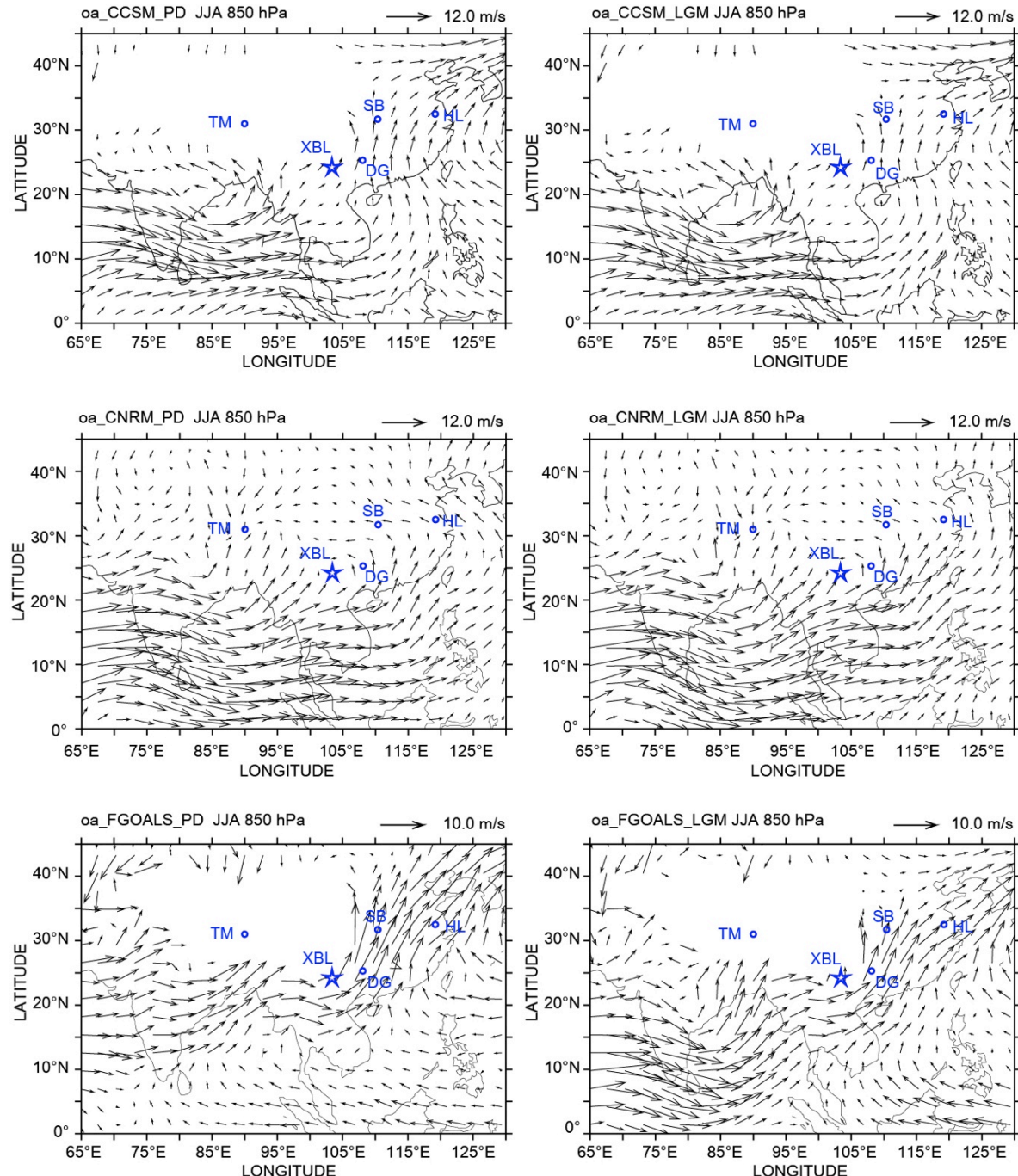


Figure S7-a. South Asia JJA 850 hPa wind for Present Day and the Last Glacial Maximum (LGM) in ocean-atmosphere coupled global circulation models (GCMs) from the PMIP2 (Paleoclimatology Modeling Intercomparison Project, Phase II) database (22). Markers indicate the locations of the following caves: XBL, Xiaobailong cave; TM, Tianmen cave; SB, Sanbao cave; DG, Dongge cave; HL, Hulu cave. Comparing the LGM to Present Day, the wind field upstream of XBL cave does not show significant change in any of the models, indicating that the Bay of Bengal was the primary source of the moisture of the XBL cave.

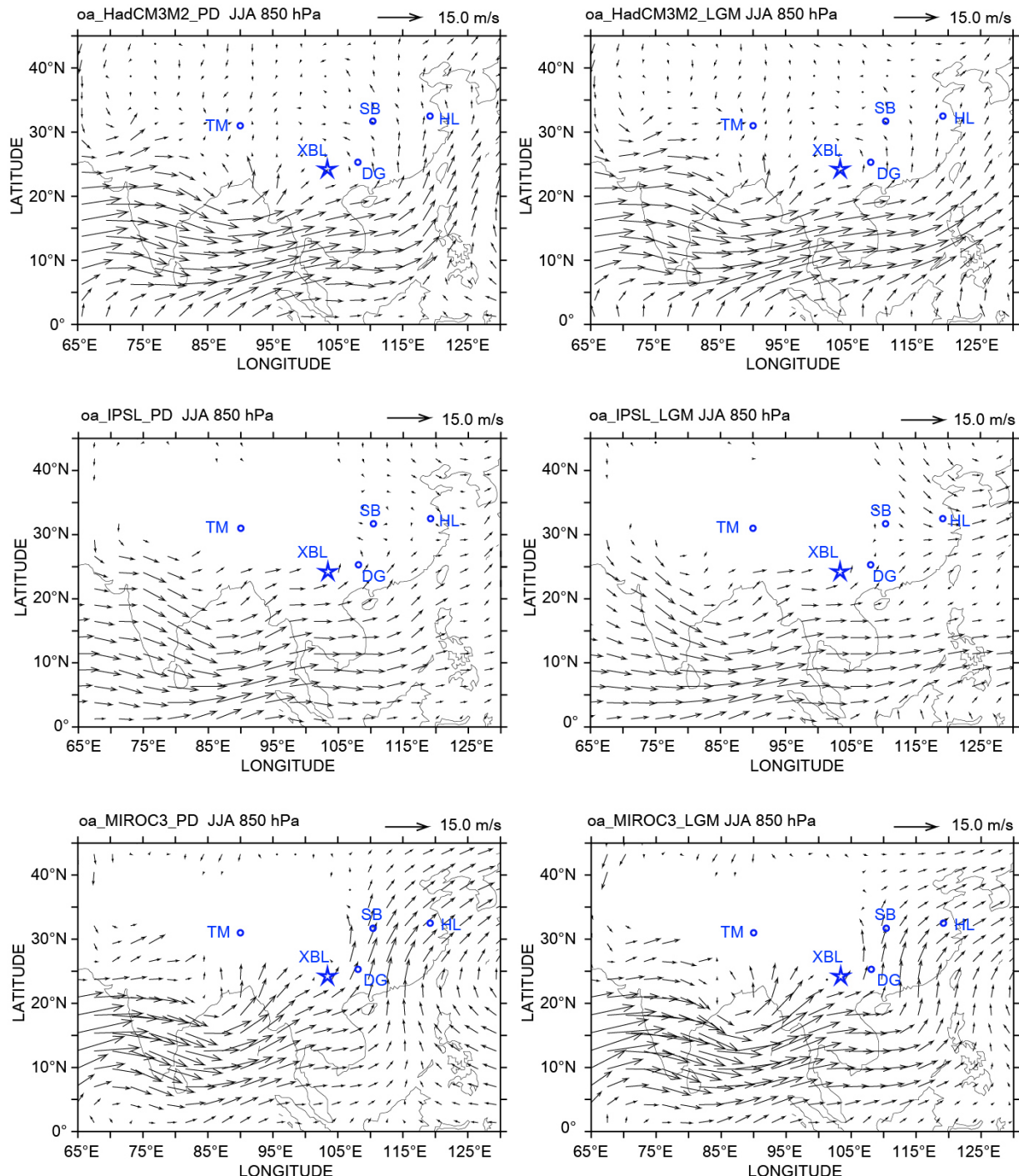


Figure S7-b. South Asia JJA 850 hPa wind for Present Day and the Last Glacial Maximum (LGM) in ocean-atmosphere coupled global circulation models (GCMs) from the PMIP2 (Paleoclimate Modeling Intercomparison Project, Phase II) database (22). Markers indicate the locations of the following caves: XBL, Xiaobailong cave; TM, Tianmen cave; SB, Sanbao cave; DG, Dongge cave; HL, Hulu cave. Comparing the LGM to Present Day, the wind field upstream of XBL cave does not show significant change in any of the models, indicating that the Bay of Bengal was the primary source of the moisture of the XBL cave.

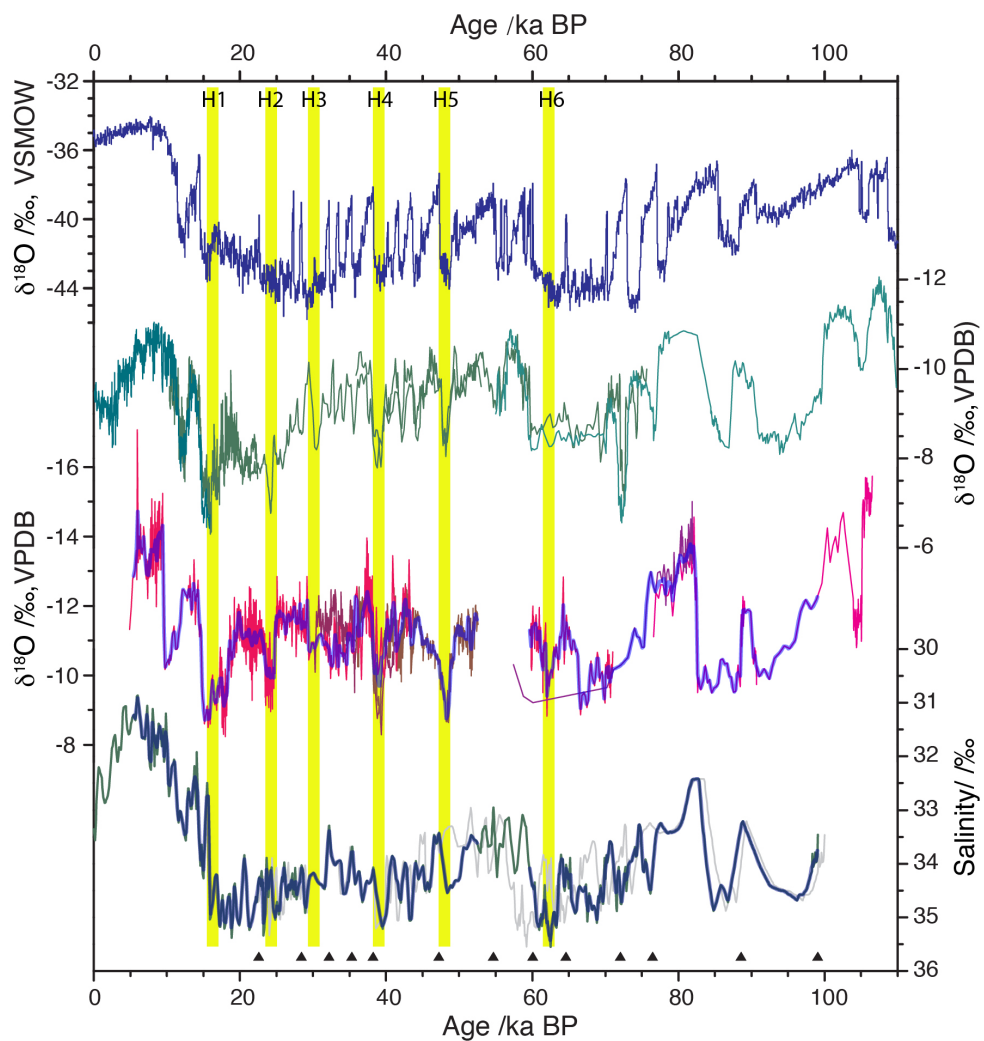


Figure S8. Comparison of speleothem  $\delta^{18}\text{O}_{\text{c}}$  records from Xiaobailong and Hulu-Dongge-Sanbao caves (17) with salinity records reconstructed from 126 KL, Bay of Bengal (4) and NGRIP ice core  $\delta^{18}\text{O}$  record (23) over the last 110 kyr. The gray line in the salinity record uses the original published chronology while the green line is a new chronology tuned to the updated NGRIP ice core record. The triangles beneath the curve indicate the tie points. The yellow bars indicate the weak monsoon intervals coincident with cold Heinrich events in North Atlantic. There is a clear visual match between the XBL  $\delta^{18}\text{O}_{\text{c}}$  and the ODP 126 KL reconstructed salinity records and the two 200-yrs smoothed records (blue thick lines) have a correlation coefficient of  $r=0.56$  ( $n=435$ ), indicating that a correlation exists between these two records on centennial to orbital time scales.

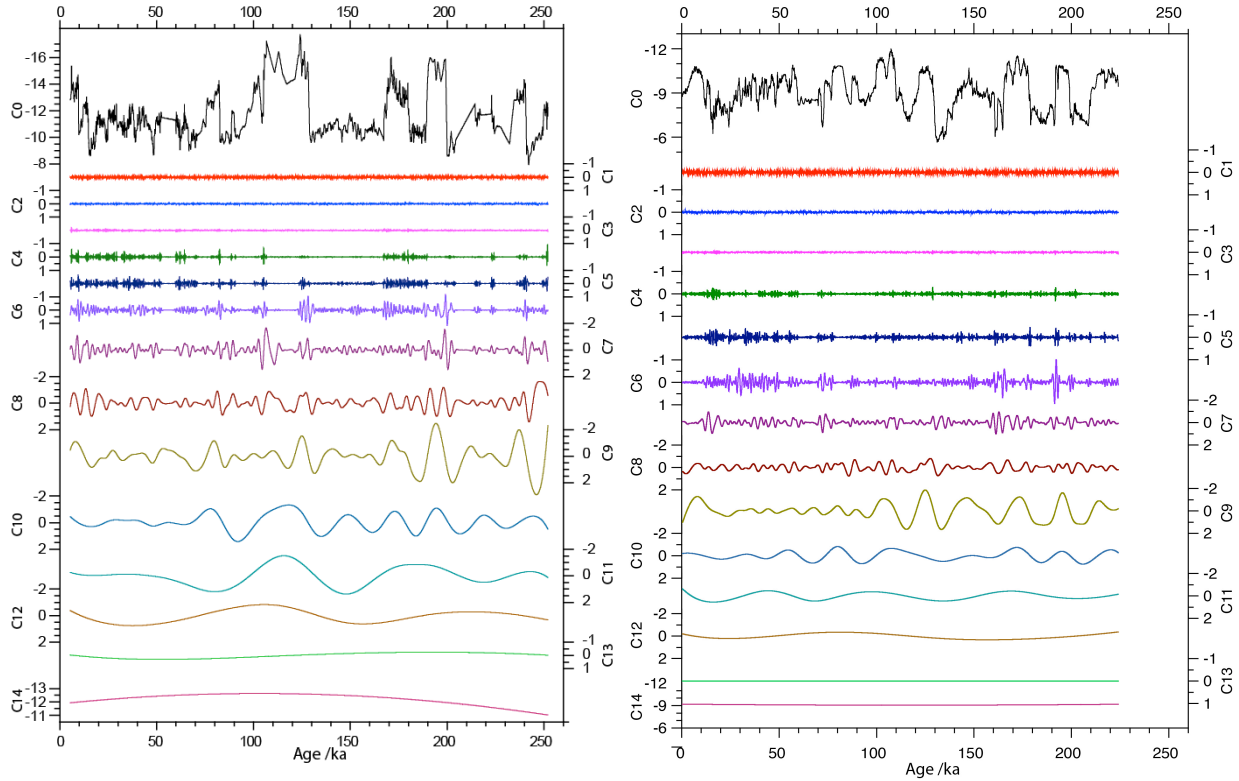


Figure S9. Intrinsic components of the ensemble empirical mode decomposition (EEMD) of the (a) XBL and (b) Hulu-Dongge-Sanbao composite  $\delta^{18}\text{O}_c$  records. We combined the different stalagmite records by interpolating each to 10 yr resolution and averaging to produce the XBL composite record. White noise of 0.4 (0.2 standard deviations of the data) and the ensemble number of 500 are used for the first EEMD decomposition. To remove high-frequency fluctuations, new time series were formed by summing components C5-14 from the first decomposition (C0 in the figure). EEMD analysis (24) was repeated for new time series with white noise of 0.4 and ensemble size of 300, producing the components shown above.

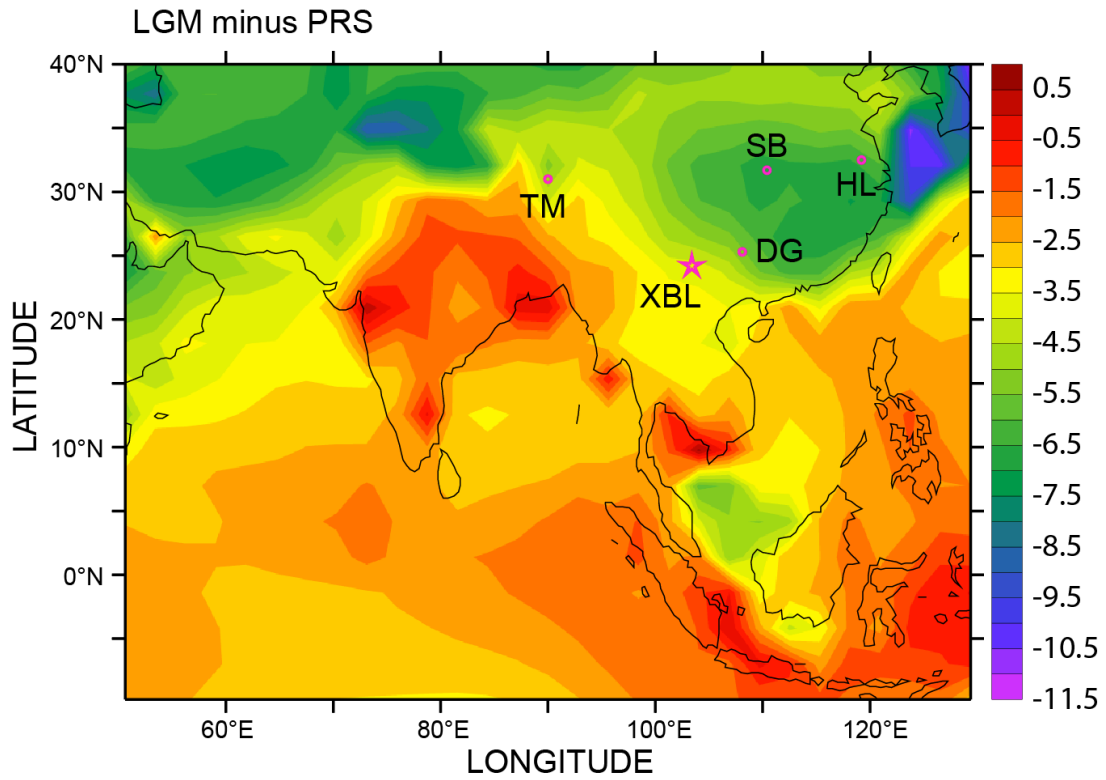


Figure S10. Modeled temperature difference between LGM and Present Day. It indicates that the temperature changes are  $\sim 4 \pm 0.5^{\circ}\text{C}$  at XBL cave,  $\sim 6 \pm 0.5^{\circ}\text{C}$  at Hulu and Sanbao caves. Here we use the  $4^{\circ}\text{C}$  and  $6^{\circ}\text{C}$  for XBL and HL-DG-SB caves respectively to calculate the speleothem calcite  $\delta^{18}\text{O}$  by using the temperature dependent fraction (25).

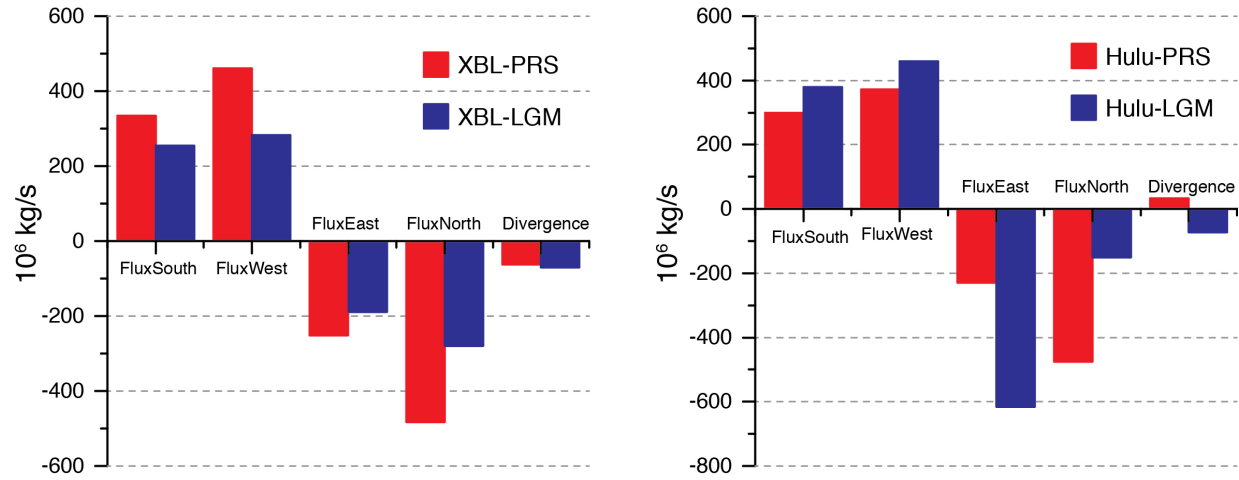


Figure S11. Vertically-integrated water vapor fluxes and divergence into and out of boxes around (a) XBL ( $100\text{-}110^\circ\text{E}$ ,  $20\text{-}30^\circ\text{N}$ ) and (b) Hulu ( $115\text{-}125^\circ\text{E}$ ,  $25\text{-}35^\circ\text{N}$ ). Present-day values are in red and LGM values are in blue. FluxSouth, FluxWest, FluxEast and FluxNorth denote integrated water vapor flux across the southern, western, eastern and northern boundaries of the boxes. Here positive values indicate fluxes into the boxes and negative values indicate fluxes out of the boxes. Unit is  $10^6 \text{ kg s}^{-1}$ .

## References

1. Dansgaard W (1964) Stable isotopes in precipitation. *Tellus* 16(4): 436-468.
2. Hu C, et al. (2008) Quantification of Holocene Asian monsoon rainfall from spatially separated cave records. *Earth and Planetary Science Letters* 266: 221-232.
3. Cai Y, et al. (2012) The Holocene Indian monsoon variability over the southern Tibetan Plateau and its teleconnections. *Earth and Planetary Science Letters* 335–336: 135-144.
4. Kudrass HR, Hofmann A, Doose H, Emeis K, Erlenkeuser H (2001) Modulation and amplification of climatic changes in the Northern Hemisphere by the Indian summer monsoon during the past 80 k.y. *Geology* 29: 63-66.
5. Collins W D, et al. (2002) Description of the NCAR Community Atmospheric Model (CAM2), 189 pp., National Center for Atmospheric Research, Boulder, Colo.
6. Lee J-E, Fung I, DePaolo DJ, Henning CC (2007) Analysis of the global distribution of water isotopes using the NCAR atmospheric general circulation model. *Journal of Geophysical Research: Atmospheres* 112: D16306.
7. Peltier WR (2004) Global glacial isostasy and the surface of the ice-age Earth: The ICE-5G (VM2) model and GRACE. *Annu Rev Earth Planet Sci* 32:111–149.
8. Otto-Bliesner B L, et al. (2006) Last Glacial Maximum and Holocene Climate in CCSM3. *Journal of Climate* 19(11): 2526-2544.
9. Pausata FSR, Battisti DS, Nisancioglu KH, Bitz CM (2011) Chinese stalagmite  $\delta^{18}\text{O}$  controlled by changes in the Indian monsoon during a simulated Heinrich event. *Nature Geoscience* 4: 474-480.
10. Boos WR, Kuang Z (2013) Sensitivity of the South Asian monsoon to elevated and non-elevated heating. *Scientific Reports* 3: 1192.
11. Lee, J-E, Fung I, DePaolo DJ, Otto-Bliesner B (2008) Water isotopes during the Last Glacial Maximum: New general circulation model calculations. *Journal of Geophysical Research: Atmospheres* 113: D19109.
12. Lee J-E, Johnson K, Fung I (2009) Precipitation over South America during the Last Glacial Maximum: An analysis of the “amount effect” with a water isotope-enabled general circulation model. *Geophysical Research Letters* 36: L19701.
13. Ding YH (2004) Seasonal march of East Asian monsoon. *East Asian monsoon*, ed Chang CP (World Scientific, Singapore), p 560.
14. Wang YJ, et al. (2001) A high-resolution absolute-dated late Pleistocene Monsoon record from Hulu cave, China. *Science* 294: 2345-2348.

15. Dykoski CA, et al. (2005) A high-resolution, absolute-dated Holocene and deglacial Asian monsoon record from Dongge Cave, China. *Earth and Planetary Science Letters* 233: 71-86.
16. Kelly MJ, et al. (2006) High resolution characterization of the Asian Monsoon between 146,000 and 99,000 years BP from Dongge Cave, China and global correlation of events surrounding Termination II. *Palaeogeography Palaeoclimatology Palaeoecology* 236: 20-38.
17. Wang, YJ, et al. (2008) Millennial- and orbital-scale changes in the East Asian monsoon over the past 224,000 years. *Nature* 451: 1090-1093.
18. Cheng H, et al. (2009) Ice Age Terminations. *Science* 326: 248-252.
19. Cai Y, et al. (2010) Large variations of oxygen isotopes in precipitation over south-central Tibet during Marine Isotope Stage 5. *Geology* 38: 243-246.
20. Sinha A, et al. (2005) Variability of Southwest Indian summer monsoon precipitation during the Bølling-Ållerød. *Geology* 33(10): 813-816.
21. Yatagai AO, et al. (2009) A 44-year daily gridded precipitation dataset for Asia based on a dense network of rain gauges, *SOLA*, 5: 137-140.
22. Braconnot P, et al. (2007) Results of PMIP2 coupled simulations of the Mid-Holocene and Last Glacial Maximum, Part 1: experiments and large-scale features. *Climate of the Past* 3: 261-277.
23. North Greenland Ice Core Project members (NGRIP members) (2004) High-resolution record of Northern Hemisphere climate extending into the last interglacial period. *Nature*, 431:147-151.
24. Wu Z, Huang NE (2009) Ensemble Empirical Mode Decomposition: A Noise-Assisted Data Analysis Method. *Advances in Adaptive Data Analysis* 01: 1-41.
25. Kim ST, O'Neil JR (1997) Equilibrium and nonequilibrium oxygen isotope effects in synthetic carbonates. *Geochim Cosmochim Ac* 61: 3461-3475.

Supplementary Table S1.  $^{230}\text{Th}$  dating results. The error is  $2\sigma$  error.

Sample Number	Distance from bottom/mm	$^{238}\text{U}$ (ppb)	$^{232}\text{Th}$ (ppt)	$^{230}\text{Th} / ^{232}\text{Th}$ (atomic $\times 10^{-6}$ )	$\delta^{234}\text{U}^*$ (measured)	$^{230}\text{Th} / ^{238}\text{U}$ (activity)	$^{230}\text{Th}$ Age (ky) (uncorrected)	$^{230}\text{Th}$ Age (ky BP)*** (corrected)	$\delta^{234}\text{U}_{\text{initial}}**$ (corrected)
XBL3-8	8	5170.8±7.1	1615±14	17080±150	34.9±1.5	0.3232±0.0008	40.79±0.15	<b>40.73±0.15</b>	39.2±1.6
XBL3-20	20	6110.7±35.2	425±7	74910±1250	36.0±2.4	0.3156±0.0020	39.59±0.33	<b>39.54±0.33</b>	40.2±2.7
XBL3-34	34	7791.5±44.2	1081±8	36390±300	37.6±2.3	0.3058±0.0020	38.04±0.31	<b>37.98±0.31</b>	41.8±2.6
XBL3-38	38	3116.8±5.3	521±10	30310±560	39.8±1.8	0.3069±0.0009	38.11±0.16	<b>38.05±0.16</b>	44.3±2.0
XBL3-55	55	138.0±0.2	1279±9	525±5	38.6±2.3	0.2946±0.0017	36.35±0.27	<b>36.04±0.30</b>	42.8±2.6
XBL3-95	95	190.2±0.2	47±8	272280±63180	43.3±1.2	0.2892±0.0010	35.39±0.15	<b>35.33±0.15</b>	47.8±1.3
XBL3-133	133	161.8±0.2	56±8	42190±18900	50.3±1.3	0.2840±0.0011	34.36±0.16	<b>34.30±0.16</b>	55.4±1.4
XBL3-173	173	170.9±0.2	210±7	3720±130	46.0±2.2	0.2774±0.0015	33.57±0.23	<b>33.48±0.23</b>	50.6±2.4
XBL3-212	212	141.0±0.2	256±8	2500±80	45.3±2.4	0.2753±0.0017	33.30±0.25	<b>33.19±0.25</b>	49.8±2.6
XBL3-249	249	115.4±0.2	156±6	3240±130	52.7±2.5	0.2655±0.0019	31.66±0.28	<b>31.57±0.28</b>	57.6±2.7
XBL3-253	253	156.5±0.2	35±10	30850±13500	52.2±1.4	0.2659±0.0012	31.76±0.17	<b>31.70±0.17</b>	57.1±1.6
XBL3-280	280	120.6±0.3	358±13	1415±51	45.2±3.6	0.2546±0.0020	30.42±0.30	<b>30.28±0.30</b>	49.2±4.0
<hr/>									
XBL7-15	15	397.9±1.0	837±6	3920±30	43.5±2.2	0.4993±0.0019	70.69±0.44	<b>70.58±0.44</b>	53.1±2.7
XBL7-37	37	427.7±0.6	485±6	7240±90	44.7±1.5	0.4967±0.0016	70.06±0.35	<b>69.97±0.35</b>	54.5±1.8
XBL7-64	64	298.0±0.4	78±7	30650±2570	55.3±1.6	0.4884±0.0018	67.41±0.38	<b>67.35±0.38</b>	66.9±2.0
XBL7-75	75	310.1±0.4	341±7	7270±140	46.3±1.5	0.4842±0.0021	67.47±0.42	<b>67.38±0.42</b>	56.0±1.8
XBL7-100	100	297.8±0.8	357±6	6460±110	47.4±2.3	0.4692±0.0020	64.53±0.43	<b>64.45±0.43</b>	56.8±2.7
XBL7-105	105	299.5±0.7	296±6	7780±160	44.0±2.1	0.4657±0.0020	64.18±0.41	<b>64.10±0.41</b>	52.8±2.5
XBL7-137	137	256.3±0.3	94±5	20280±1040	40.6±1.5	0.4501±0.0016	61.60±0.32	<b>61.54±0.32</b>	48.3±1.8
XBL7-186	186	3793.4±13.0	122±6	231030±11100	50.7±1.6	0.4516±0.0018	61.02±0.35	<b>60.96±0.35</b>	60.3±1.9
XBL7-215	215	4328.6±30.6	190±6	170620±5020	53.8±2.9	0.4533±0.0035	61.06±0.68	<b>61.00±0.68</b>	64.0±3.4
XBL7-244	244	1886.7±13.1	121±5	112710±4490	35.9±3.0	0.4368±0.0033	59.57±0.65	<b>59.51±0.65</b>	42.5±3.5
<hr/>									
XBL65-4	4	131.0±0.1	104±2	17650±370	57.8±1.3	0.8466±0.0014	170.8±0.9	<b>170.8±0.9</b>	93.7±2.2
XBL65-66	66	135.3±0.1	42±1	44410±990	54.5±1.4	0.8418±0.0013	170.1±0.9	<b>170.0±0.9</b>	88.1±2.2
XBL65-104	104	159.6±0.2	65±1	34200±720	55.0±1.4	0.8422±0.0015	170.0±1.0	<b>170.0±1.0</b>	88.9±2.3
XBL65-147	147	150.7±0.2	72±2	28960±620	58.9±1.4	0.8435±0.0014	168.9±0.9	<b>168.8±0.9</b>	94.9±2.3
XBL65-215	215	185.9±0.2	111±2	23170±480	58.8±1.4	0.8429±0.0020	168.7±1.1	<b>168.6±1.1</b>	94.6±2.3
XBL65-244	244	197.9±0.2	103±2	26560±560	51.6±1.3	0.8344±0.0012	167.9±0.8	<b>167.8±0.8</b>	82.8±2.2
<hr/>									
XBL27-5	5	221.4±0.5	53±9	59540±9710	36.8±2.2	0.8607±0.0035	189.4±2.4	<b>189.4±2.4</b>	62.8±3.7
XBL27-43	43	231.2±0.3	238±5	13740±280	40.4±1.5	0.8582±0.0014	185.7±1.1	<b>185.6±1.1</b>	68.2±2.5
XBL27-121	121	214.8±0.2	200±4	15250±310	44.2±1.4	0.8594±0.0014	184.2±1.1	<b>184.1±1.1</b>	74.4±2.4
XBL27-167	167	111.1±0.1	108±2	14520±300	43.0±1.4	0.8541±0.0014	182.0±1.1	<b>181.9±1.1</b>	71.8±2.3
XBL27-213	213	80.6±0.2	22±8	52470±20030	48.0±2.9	0.8528±0.0041	178.9±2.6	<b>178.9±2.6</b>	79.6±4.8
XBL27-267	267	57.5±0.0	153±3	5240±110	40.9±1.4	0.8428±0.0016	177.1±1.1	<b>177.0±1.1</b>	67.5±2.3
XBL27-302	302	68.6±0.1	46±1	20630±460	40.6±1.4	0.8422±0.0016	177.0±1.1	<b>176.9±1.1</b>	66.9±2.3
XBL27-357	357	34.0±0.1	47±6	9890±1260	40.5±3.4	0.8338±0.0049	172.9±2.9	<b>172.9±2.9</b>	66.0±5.5
<hr/>									
XBL26-0.5	1	99.8±0.2	867±3	1780±10	28.8±2.1	0.9342±0.0033	252.6±4.3	<b>252.3±4.3</b>	58.7±4.4
XBL26-39	39	116.1±0.2	276±3	6430±80	25.0±2.7	0.9262±0.0036	248.8±4.8	<b>248.7±4.8</b>	50.4±5.4
XBL26-74	74	95.7±0.2	61±3	23900±1060	24.9±2.6	0.9184±0.0032	241.3±4.1	<b>241.2±4.1</b>	49.2±5.2
XBL26-82	82	205.8±0.4	31±2	101480±7830	25.6±2.6	0.9181±0.0031	240.2±4.0	<b>240.1±4.0</b>	50.5±5.2
XBL26-99	99	3377.4±14.3	53±3	973870±49520	30.5±2.4	0.9239±0.0046	240.5±5.0	<b>240.4±5.0</b>	60.2±4.7
XBL26-122	122	107.2±0.3	83±6	19570±1420	22.9±2.6	0.9170±0.0040	242.0±4.8	<b>241.9±4.8</b>	45.4±5.2
XBL26-123	123	172.7±0.2	409±5	6340±80	25.1±1.9	0.9092±0.0032	232.6±3.4	<b>232.4±3.4</b>	48.5±3.6
XBL26-125	125	171.3±0.3	625±3	4130±20	24.8±2.9	0.9123±0.0033	235.7±4.1	<b>235.5±4.1</b>	48.3±5.6
XBL26-135	135	226.7±0.3	696±8	4860±60	28.8±1.9	0.9036±0.0029	224.5±2.9	<b>224.3±2.9</b>	54.3±3.6
XBL26-168	168	61.3±0.2	1488±7	621±4	32.8±3.3	0.9133±0.0048	228.9±5.1	<b>228.1±5.0</b>	62.5±6.4
XBL26-170	170	222.0±0.4	225±3	14630±210	26.7±2.6	0.8989±0.0032	222.6±3.4	<b>222.5±3.4</b>	50.1±5.0

Table S1. (Cont.)

Sample Number	Distance from bottom/mm	$^{238}\text{U}$ (ppb)	$^{232}\text{Th}$ (ppt)	$^{230}\text{Th} / ^{232}\text{Th}$ (atomic x10 <sup>-6</sup> )	$\delta^{234}\text{U}^*$ (measured)	$^{230}\text{Th} / ^{238}\text{U}$ (activity)	$^{230}\text{Th}$ Age (ky) (uncorrected)	$^{230}\text{Th}$ Age (ky BP)*** (corrected)	$\delta^{234}\text{U}_{\text{Initial}}**$ (corrected)
XBL26-178	178	157.0±0.2	639±6	3630±40	28.5±1.7	0.8933±0.0029	216.6±2.6	<b>216.5±2.6</b>	52.6±3.2
XBL26-184	184	152.8±0.3	1493±10	1510±10	28.9±2.1	0.8945±0.0035	217.3±3.2	<b>217.0±3.2</b>	53.3±4.0
XBL26-189	189	136.2±0.3	460±6	4390±60	37.0±2.4	0.8997±0.0029	214.6±2.8	<b>214.5±2.8</b>	67.9±4.4
XBL26-197	197	300.8±0.5	112±9	39500±3080	42.1±2.0	0.8894±0.0026	203.8±2.2	<b>203.7±2.2</b>	74.9±3.5
XBL26-211	211	244.9±0.3	19±7	188380±67760	39.3±1.6	0.8836±0.0031	201.9±2.3	<b>201.9±2.3</b>	69.6±2.9
XBL26-251	251	228.7±0.3	19±7	171340±59670	41.1±1.6	0.8846±0.0029	201.3±2.1	<b>201.3±2.1</b>	72.6±2.9
XBL26-262	262	97.9±0.1	50±10	28690±5990	39.2±1.8	0.8819±0.0024	200.9±2.0	<b>200.8±2.0</b>	69.2±3.1
XBL26-294	294	152.1±0.2	25±5	85260±18330	37.8±1.8	0.8580±0.0028	187.3±1.9	<b>187.3±1.9</b>	64.1±3.2
XBL26-366	366	193.0±0.3	73±7	36580±3570	29.8±2.1	0.8419±0.0029	182.7±2.0	<b>182.6±2.0</b>	50.0±3.5
XBL26-402	402	177.5±0.3	178±5	13950±380	38.3±2.1	0.8456±0.0030	180.1±2.0	<b>180.0±2.0</b>	63.7±3.6
XBL26-414	414	110.1±0.2	77±8	19660±1960	35.4±2.0	0.8330±0.0024	175.0±1.6	<b>175.0±1.6</b>	58.1±3.2
XBL26-434	434	66.5±0.2	32±6	27860±5480	37.8±4.5	0.8249±0.0044	169.8±3.0	<b>169.7±3.0</b>	61.1±7.3
XBL26-466	466	43.1±0.1	90±6	6630±450	39.0±3.8	0.8357±0.0047	174.7±3.0	<b>174.6±3.0</b>	63.8±6.2
XBL26-469	469	71.9±0.1	1935±11	511±4	41.2±1.7	0.8320±0.0042	171.7±2.2	<b>170.9±2.2</b>	66.9±2.8
XBL26-474	474	102.7±0.1	156±6	8830±340	40.9±2.5	0.8099±0.0039	161.5±2.0	<b>161.4±2.0</b>	64.5±4.0
XBL26-504	504	50.8±0.1	120±6	5320±290	43.5±3.8	0.7621±0.0054	140.9±2.4	<b>140.8±2.4</b>	64.8±5.7
XBL26-524	524	100.6±0.1	65±7	17980±1900	38.3±2.5	0.7063±0.0047	123.2±1.6	<b>123.1±1.6</b>	54.3±3.6
XBL26-535	535	96.2±0.1	286±6	2940±70	39.0±2.7	0.5295±0.0050	77.4±1.1	<b>77.2±1.1</b>	48.5±3.3
<hr/>									
XBL48-13	13	313.4±0.8	871±3	4060±20	85.2±3.4	0.6840±0.0031	106.66±1.02	<b>106.54±1.02</b>	115.1±4.7
XBL48-34	34	285.0±0.4	90±5	35840±2090	87.4±1.7	0.6818±0.0020	105.69±0.59	<b>105.62±0.59</b>	117.9±2.2
XBL48-56	56	389.9±0.8	30±3	143870±13880	87.8±3.0	0.6773±0.0035	104.46±1.04	<b>104.40±1.04</b>	118.0±4.0
XBL48-67	67	396.1±0.9	200±3	21740±370	78.0±3.0	0.6643±0.0025	102.76±0.83	<b>102.69±0.83</b>	104.3±4.0
XBL48-73	73	201.3±0.6	53±3	41200±2250	75.5±5.4	0.6528±0.0037	100.43±1.30	<b>100.37±1.29</b>	100.3±7.2
XBL48-81	81	217.9±0.5	245±4	9150±150	69.2±3.4	0.6248±0.0029	94.52±0.86	<b>94.43±0.86</b>	90.3±4.4
XBL48-86	86	294.4±0.6	227±4	12850±210	57.2±3.1	0.6011±0.0026	90.75±0.76	<b>90.67±0.76</b>	73.8±4.0
XBL48-102	102	358.1±0.8	90±2	39450±1010	63.5±2.9	0.6032±0.0027	90.44±0.76	<b>90.37±0.76</b>	82.0±3.7
XBL48-108	108	283.2±0.5	110±3	25530±600	70.4±2.7	0.6023±0.0027	89.24±0.72	<b>89.17±0.72</b>	90.6±3.4
XBL48-126	126	267.3±0.6	372±3	7070±60	66.6±3.0	0.5971±0.0025	88.47±0.71	<b>88.37±0.71</b>	85.5±3.9
XBL48-165	165	229.2±0.5	216±3	9910±150	60.9±3.1	0.5673±0.0028	82.65±0.72	<b>82.57±0.72</b>	76.9±3.9
XBL48-200	200	216.1±0.3	87±4	22230±1030	64.1±1.6	0.5418±0.0018	77.00±0.41	<b>76.93±0.41</b>	79.7±2.0
<hr/>									
XBL4-1	1	293.0±0.4	566±7	4970±70	90.5±2.2	0.5814±0.0029	82.06±0.66	<b>81.95±0.66</b>	114.2±2.7
XBL4-80	80	264.3±0.3	109±6	22600±1170	80.6±1.4	0.5667±0.0021	80.22±0.46	<b>80.15±0.46</b>	101.1±1.8
XBL4-150	150	299.1±0.4	526±9	5360±100	75.1±2.3	0.5713±0.0024	81.84±0.58	<b>81.74±0.58</b>	94.6±3.0
XBL4-203	203	295.9±0.4	71±6	38990±3290	79.4±1.6	0.5645±0.0020	79.90±0.46	<b>79.84±0.46</b>	99.5±2.0
XBL4-237	237	780.0±0.8	816±12	9120±140	120.7±1.9	0.5776±0.0022	77.82±0.47	<b>77.74±0.47</b>	150.4±2.4
XBL4-263	263	266.2±0.4	1112±6	2062±14	57.1±1.6	0.5217±0.0020	73.71±0.43	<b>73.54±0.43</b>	70.3±2.0
XBL4-270	270	475.9±0.7	810±5	5011±37	81.0±1.4	0.5169±0.0018	70.31±0.36	<b>70.21±0.36</b>	98.8±1.7
XBL4-272	272	209.5±0.3	2429±23	651±7	65.3±3.8	0.4572±0.0027	60.81±0.57	<b>60.44±0.59</b>	77.5±4.5
XBL4-275	275	162.7±0.2	133±5	9050±330	73.4±2.2	0.4476±0.0020	58.50±0.38	<b>58.42±0.38</b>	86.6±2.6
<hr/>									
XBL29-39	39	63.7±0.1	447±7	803±14	41.0±3.3	0.3410±0.0033	43.21±0.54	<b>42.96±0.55</b>	46.3±3.8
XBL29-69	69	57.6±0.1	217±4	1351±28	38.3±2.3	0.3082±0.0009	38.31±0.17	<b>38.14±0.18</b>	42.7±2.6
XBL29-95	95	13.8±0.0	82±6	844±63	40.9±4.6	0.3031±0.0034	37.49±0.54	<b>37.27±0.55</b>	45.5±5.1
XBL29-112	112	34.3±0.0	45±1	3812±93	46.8±1.5	0.3045±0.0010	37.39±0.16	<b>37.29±0.16</b>	52.0±1.6
XBL29-168	168	35.5±0.1	447±9	348±8	44.6±3.1	0.2662±0.0034	32.00±0.48	<b>31.59±0.54</b>	48.7±3.4
XBL29-173	173	39.0±0.0	65±1	2429±53	44.6±1.4	0.2467±0.0009	29.32±0.13	<b>29.22±0.14</b>	48.4±1.5
XBL29-195	195	47.1±0.0	66±1	2771±62	37.5±1.7	0.2366±0.0010	28.17±0.15	<b>28.08±0.15</b>	40.6±1.8
XBL29-216	216	21.9±0.1	118±6	689±36	42.9±3.5	0.2258±0.0024	26.60±0.34	<b>26.39±0.34</b>	46.3±3.7
XBL29-275	275	58.9±0.1	82±3	2442±93	40.4±4.5	0.2068±0.0025	24.16±0.34	<b>24.06±0.34</b>	43.2±4.9
XBL29-338	338	9.3±0.0	21±6	1448±419	50.2±4.5	0.1958±0.0032	22.50±0.42	<b>22.38±0.42</b>	53.4±4.8

Table S1. (Cont.)

Sample Number	Distance from bottom/mm	$^{238}\text{U}$ (ppb)	$^{232}\text{Th}$ (ppt)	$^{230}\text{Th} / ^{232}\text{Th}$ (atomic $\times 10^{-6}$ )	$\delta^{234}\text{U}^*$ (measured)	$^{230}\text{Th} / ^{238}\text{U}$ (activity)	$^{230}\text{Th}$ Age (ky) (uncorrected)	$^{230}\text{Th}$ Age (ky BP)*** (corrected )	$\delta^{234}\text{U}_{\text{initial}}^*$ (corrected)
XBL29-403	403	59.0 $\pm$ 0.1	594 $\pm$ 3	311 $\pm$ 4	39.8 $\pm$ 3.9	0.1899 $\pm$ 0.0022	21.99 $\pm$ 0.30	<b>21.65<math>\pm</math>0.33</b>	42.3 $\pm$ 4.2
XBL29-463	463	93.8 $\pm$ 0.2	2990 $\pm$ 9	100 $\pm$ 1	51.9 $\pm$ 2.6	0.1921 $\pm$ 0.0016	21.99 $\pm$ 0.21	<b>21.05<math>\pm</math>0.49</b>	55.1 $\pm$ 2.8
XBL29-473	473	72.2 $\pm$ 0.1	6699 $\pm$ 40	37 $\pm$ 1	43.3 $\pm$ 2.5	0.2051 $\pm$ 0.0042	23.86 $\pm$ 0.55	<b>21.20<math>\pm</math>1.43</b>	46.0 $\pm$ 2.6
XBL29-555	555	15.1 $\pm$ 0.0	296 $\pm$ 6	120 $\pm$ 3	34.6 $\pm$ 4.4	0.1429 $\pm$ 0.0026	16.22 $\pm$ 0.33	<b>15.61<math>\pm</math>0.43</b>	36.1 $\pm$ 4.6
XBL29-561	561	58.6 $\pm$ 0.2	1290 $\pm$ 6	89 $\pm$ 2	31.0 $\pm$ 4.7	0.1190 $\pm$ 0.0028	13.38 $\pm$ 0.35	<b>12.70<math>\pm</math>0.46</b>	32.1 $\pm$ 4.9
XBL29-564	564	26.1 $\pm$ 0.1	1424 $\pm$ 5	30 $\pm$ 1	41.5 $\pm$ 5.6	0.1005 $\pm$ 0.0040	11.08 $\pm$ 0.46	<b>9.48<math>\pm</math>0.90</b>	42.7 $\pm$ 5.7
XBL29-588	588	153.2 $\pm$ 0.4	1679 $\pm$ 5	112 $\pm$ 2	45.2 $\pm$ 3.1	0.0746 $\pm$ 0.0010	8.08 $\pm$ 0.12	<b>7.72<math>\pm</math>0.19</b>	46.2 $\pm$ 3.2
XBL29-595	595	162.3 $\pm$ 0.3	1882 $\pm$ 7	85 $\pm$ 1	43.7 $\pm$ 2.0	0.0600 $\pm$ 0.0006	6.46 $\pm$ 0.07	<b>6.08<math>\pm</math>0.17</b>	44.5 $\pm$ 2.0

\* $\delta^{234}\text{U} = ([^{234}\text{U}/^{238}\text{U}]_{\text{activity}} - 1) \times 1000$ . \*\*  $\delta^{234}\text{U}_{\text{initial}}$  was calculated based on  $^{230}\text{Th}$  age (T), i.e.,  $\delta^{234}\text{U}_{\text{initial}} = \delta^{234}\text{U}_{\text{measured}} \times e^{\lambda^{234} \times T}$ . Corrected  $^{230}\text{Th}$  ages assume the initial  $^{230}\text{Th}/^{232}\text{Th}$  atomic ratio of  $4.4 \pm 2.2 \times 10^{-6}$ . Those are the values for a material at secular equilibrium, with the bulk earth  $^{232}\text{Th}/^{238}\text{U}$  value of 3.8. The errors are arbitrarily assumed to be 50%. \*\*\*B.P. stands for “Before Present” where the “Present” is defined as the year 1950 A.D.

Supplementary Table S2. Oxygen isotopic data of stalagmites from Xiaobailong Cave. Depths are relative to the bottom (oldest end) of the stalagmites and are measured along the growth axis. Ages are linearly interpolated between  $^{230}\text{Th}$  dates (see Table S1).

Distance (mm)	Age (ky, BP)	$\delta^{18}\text{O}$ (‰, VPDB)									
<b>XBL-29</b>											
598.18	5.34	-12.79	585.35	7.92	-13.54	568.32	9.20	-13.03	559.80	13.46	-11.83
597.30	5.54	-12.89	585.00	7.94	-13.42	567.95	9.22	-14.30	559.60	13.55	-12.41
596.85	5.65	-13.01	584.55	7.98	-15.08	567.58	9.25	-13.89	559.40	13.64	-12.44
596.41	5.75	-13.45	584.11	8.01	-12.85	567.20	9.28	-14.08	559.19	13.73	-13.33
595.97	5.85	-13.61	583.66	8.04	-13.09	566.83	9.31	-14.50	558.99	13.82	-12.26
595.75	5.91	-13.14	583.21	8.08	-13.37	566.46	9.34	-14.25	558.79	13.91	-11.46
595.66	5.93	-12.75	582.77	8.11	-14.34	566.08	9.36	-14.89	558.59	14.00	-12.28
595.53	5.96	-16.22	582.32	8.15	-13.64	565.71	9.39	-14.57	558.39	14.09	-12.35
595.44	5.98	-17.08	581.88	8.18	-12.91	565.34	9.42	-14.56	558.19	14.18	-12.26
595.31	6.01	-15.64	581.43	8.21	-13.28	564.96	9.45	-15.24	557.98	14.27	-12.74
595.22	6.03	-15.37	580.98	8.25	-13.70	564.88	9.46	-14.83	557.78	14.36	-11.92
595.09	6.06	-13.82	580.54	8.28	-13.81	564.75	9.46	-14.67	557.58	14.45	-11.11
595.00	6.08	-13.36	580.09	8.31	-13.70	564.67	9.47	-13.90	557.38	14.54	-11.31
594.89	6.11	-13.24	579.67	8.34	-13.58	564.55	9.48	-13.47	557.18	14.64	-11.47
594.81	6.12	-13.64	579.26	8.37	-15.00	564.46	9.52	-13.57	556.98	14.73	-10.83
594.70	6.15	-13.65	578.85	8.41	-14.54	564.34	9.66	-10.46	556.77	14.82	-9.55
594.33	6.24	-14.01	578.44	8.44	-12.65	564.26	9.75	-10.17	556.57	14.91	-9.33
593.96	6.32	-13.35	578.03	8.47	-14.00	564.13	9.88	-10.25	556.37	15.00	-9.17
593.59	6.41	-14.36	577.62	8.50	-14.40	564.05	9.97	-10.38	555.97	15.18	-8.60
593.22	6.50	-13.50	577.21	8.53	-13.78	563.93	10.10	-10.39	555.16	15.54	-9.12
592.85	6.58	-13.68	576.80	8.56	-12.66	563.84	10.19	-10.47	554.30	15.65	-8.50
592.48	6.67	-13.48	576.39	8.59	-11.98	563.72	10.32	-10.30	553.44	15.71	-8.57
592.11	6.76	-13.64	575.98	8.62	-13.02	563.64	10.41	-10.59	552.57	15.76	-9.03
591.74	6.84	-14.29	575.57	8.65	-13.89	563.51	10.54	-10.43	551.70	15.82	-8.82
591.37	6.93	-13.89	575.16	8.68	-13.13	563.31	10.76	-11.10	550.83	15.87	-8.70
591.00	7.02	-13.53	574.75	8.71	-14.17	563.10	10.99	-11.42	549.96	15.93	-8.65
590.63	7.10	-13.00	574.34	8.74	-14.73	562.89	11.21	-10.74	549.05	15.98	-8.59
590.26	7.19	-12.77	573.93	8.78	-13.56	562.69	11.43	-10.75	548.15	16.04	-9.38
589.90	7.28	-13.34	573.51	8.81	-13.46	562.48	11.65	-11.26	547.25	16.10	-9.68
589.55	7.36	-12.21	573.10	8.84	-14.07	562.27	11.87	-11.53	546.35	16.16	-9.91
589.20	7.44	-13.29	572.69	8.87	-13.03	562.07	12.10	-12.45	545.45	16.21	-9.89
588.85	7.52	-12.79	572.27	8.90	-14.81	561.86	12.32	-12.47	544.59	16.27	-10.01
588.50	7.60	-13.50	571.86	8.93	-15.01	561.65	12.54	-12.36	543.77	16.32	-9.52
588.15	7.68	-12.84	571.45	8.96	-14.63	561.45	12.73	-12.29	542.95	16.37	-9.45
587.80	7.73	-13.23	571.03	8.99	-13.50	561.24	12.82	-12.14	542.13	16.42	-9.54
587.45	7.76	-13.21	570.62	9.02	-15.00	561.03	12.91	-12.40	541.31	16.47	-9.27
587.10	7.79	-14.22	570.21	9.05	-13.70	560.83	13.00	-12.59	540.49	16.53	-9.23
586.75	7.81	-13.07	569.81	9.08	-13.38	560.62	13.10	-12.25	539.66	16.58	-9.14
586.40	7.84	-14.55	569.44	9.11	-13.89	560.41	13.19	-12.87	538.82	16.63	-9.24
586.05	7.87	-13.34	569.07	9.14	-14.08	560.21	13.28	-12.26	537.98	16.69	-9.33
585.70	7.89	-13.32	568.69	9.17	-13.60	560.00	13.37	-11.74	537.14	16.74	-9.23

Continue to next page

Supplementary Table S2 (Cont.)

Distance (mm)	Age (ky, BP)	$\delta^{18}\text{O}$ (‰, VPDB)									
536.30	16.79	-9.17	504	18.84	-9.95	457	21.11	-11.29	410	21.58	-10.32
535.46	16.84	-8.99	503	18.90	-10.23	456	21.12	-11.41	409	21.59	-10.87
534.61	16.90	-9.50	502	18.96	-10.67	455	21.13	-11.13	408	21.60	-9.87
533.73	16.95	-9.69	501	19.03	-10.27	454	21.14	-10.93	407	21.61	-11.65
532.85	17.01	-9.62	500	19.09	-10.71	453	21.15	-11.30	406	21.62	-11.25
531.97	17.07	-9.72	499	19.15	-10.91	452	21.16	-11.11	405	21.63	-10.80
531.10	17.12	-9.49	498	19.22	-12.25	451	21.17	-11.19	404	21.64	-10.59
530.22	17.18	-9.37	497	19.28	-10.52	450	21.18	-10.74	403	21.65	-11.24
529.43	17.23	-9.65	496	19.34	-11.24	449	21.19	-11.53	402	21.67	-9.28
528.67	17.27	-10.32	495	19.41	-11.08	448	21.20	-11.31	401	21.68	-10.93
527.92	17.32	-10.81	494	19.47	-11.06	447	21.21	-11.92	400	21.69	-11.61
527.16	17.37	-9.90	493	19.53	-10.65	446	21.22	-10.75	399	21.70	-11.48
526.40	17.42	-9.41	492	19.60	-11.92	445	21.23	-11.81	398	21.71	-10.46
525.64	17.47	-9.96	491	19.66	-11.30	444	21.24	-11.20	397	21.72	-11.76
524.86	17.52	-10.53	490	19.72	-11.07	443	21.25	-11.96	396	21.73	-10.85
523.91	17.58	-8.49	489	19.79	-12.05	442	21.26	-11.29	395	21.74	-10.70
522.95	17.64	-10.11	488	19.85	-12.03	441	21.27	-11.56	394	21.75	-10.02
522.00	17.70	-9.73	487	19.91	-11.80	440	21.28	-11.09	393	21.77	-11.38
521.05	17.76	-8.30	486	19.97	-10.99	439	21.29	-10.68	392	21.78	-10.54
520.10	17.82	-9.69	485	20.04	-11.79	438	21.30	-11.44	391	21.79	-10.56
519.18	17.88	-9.04	484	20.10	-11.90	437	21.31	-12.55	390	21.80	-10.42
518.27	17.93	-8.80	483	20.16	-11.26	436	21.32	-11.43	389	21.81	-11.53
517.82	17.96	-9.30	482	20.23	-11.05	435	21.33	-10.91	388	21.82	-10.75
517.36	17.99	-10.18	481	20.29	-10.84	434	21.34	-10.81	387	21.83	-11.52
516.91	18.02	-8.23	480	20.35	-11.70	433	21.35	-10.18	386	21.84	-11.09
516.46	18.05	-9.48	479	20.42	-10.81	432	21.36	-11.44	385	21.86	-11.12
515.55	18.11	-9.78	478	20.48	-11.09	431	21.37	-10.44	384	21.87	-12.19
514.53	18.17	-8.83	477	20.54	-10.67	430	21.38	-11.94	383	21.88	-10.50
513.35	18.24	-9.81	476	20.61	-10.79	429	21.39	-11.77	382	21.89	-10.61
513.00	18.27	-10.00	475	20.67	-11.08	428	21.40	-11.64	381	21.90	-11.51
512.18	18.32	-9.57	474	20.73	-12.12	427	21.41	-11.07	380	21.91	-11.26
512.00	18.33	-9.40	473	20.80	-11.64	426	21.42	-11.59	379	21.92	-11.51
511.50	18.39	-10.21	472	20.82	-10.63	425	21.43	-10.12	378	21.93	-11.11
510.80	18.39	-10.78	471	20.85	-10.32	424	21.44	-10.99	377	21.95	-11.65
510.00	18.46	-10.50	470	20.87	-11.43	423	21.45	-10.48	376	21.96	-10.99
509.86	18.46	-10.68	469	20.90	-11.08	422	21.46	-10.90	375	21.97	-11.81
509.00	18.52	-10.73	468	20.92	-11.04	421	21.47	-10.61	374	21.98	-11.19
508.94	18.52	-10.13	467	20.95	-11.08	420	21.48	-10.89	373	21.99	-11.53
508.01	18.58	-10.81	466	20.97	-11.31	419	21.49	-10.55	372	22.00	-11.61
508.00	18.58	-10.75	465	21.00	-10.71	418	21.50	-12.50	371	22.01	-11.26
507.08	18.64	-11.31	464	21.02	-11.63	417	21.51	-10.86	370	22.02	-12.11
507.00	18.65	-11.73	463	21.05	-10.99	416	21.52	-10.87	369	22.04	-11.08
506.16	18.70	-10.99	462	21.06	-11.16	415	21.53	-10.77	368	22.05	-11.66
506.00	18.71	-10.56	461	21.07	-10.74	414	21.54	-10.94	367	22.06	-10.72
505.23	18.76	-11.12	460	21.08	-11.22	413	21.55	-11.86	366	22.07	-10.37
504.79	18.77	-11.42	459	21.09	-11.30	412	21.56	-10.66	365	22.08	-10.73
504.38	18.77	-11.40	458	21.10	-11.10	411	21.57	-10.86	364	22.09	-10.75

Continue to next page

Supplementary Table S2 (Cont.)

Distance (mm)	Age (ky, BP)	$\delta^{18}\text{O}$ (‰, VPDB)									
363	22.10	-10.50	316	22.97	-11.59	269	24.32	-10.18	222	26.15	-11.55
362	22.11	-11.51	315	23.00	-10.66	268	24.36	-10.41	221	26.19	-11.01
361	22.12	-11.49	314	23.03	-11.05	267	24.40	-10.45	220	26.23	-11.01
360	22.14	-11.33	313	23.05	-10.73	266	24.43	-9.04	219	26.27	-11.31
359	22.15	-11.96	312	23.08	-10.96	265	24.47	-10.07	218	26.31	-11.07
358	22.16	-10.60	311	23.11	-11.02	264	24.51	-10.18	217	26.35	-11.43
357	22.17	-10.86	310	23.14	-11.37	263	24.55	-10.23	216	26.39	-12.13
356	22.18	-10.50	309	23.16	-10.58	262	24.59	-9.70	215	26.47	-11.22
355	22.19	-10.88	308	23.19	-11.23	261	24.63	-9.62	214	26.55	-11.68
354	22.20	-11.14	307	23.22	-10.61	260	24.67	-10.03	213	26.64	-11.80
353	22.21	-11.13	306	23.24	-10.66	259	24.71	-10.05	212	26.72	-11.85
352	22.23	-12.16	305	23.27	-11.28	258	24.75	-10.05	211	26.80	-11.38
351	22.24	-11.57	304	23.30	-10.91	257	24.79	-11.55	210	26.88	-11.62
350	22.25	-10.13	303	23.32	-10.80	256	24.83	-11.10	209	26.97	-11.99
349	22.26	-11.04	302	23.35	-10.61	255	24.86	-11.50	208	27.05	-11.82
348	22.27	-10.26	301	23.38	-10.60	254	24.90	-11.70	207	27.13	-10.84
347	22.28	-11.14	300	23.40	-10.90	253	24.94	-11.25	206	27.21	-11.61
346	22.29	-10.40	299	23.43	-11.21	252	24.98	-11.12	205	27.29	-12.25
345	22.30	-10.71	298	23.46	-9.37	251	25.02	-12.00	204	27.38	-11.65
344	22.32	-10.49	297	23.49	-10.63	250	25.06	-11.24	203	27.46	-12.16
343	22.33	-10.67	296	23.51	-9.13	249	25.10	-12.85	202	27.54	-11.89
342	22.34	-10.88	295	23.54	-9.90	248	25.14	-12.03	201	27.62	-12.10
341	22.35	-11.23	294	23.57	-9.80	247	25.18	-11.15	200	27.71	-10.54
340	22.36	-10.91	293	23.59	-10.93	246	25.22	-11.96	199	27.79	-11.46
339	22.37	-11.00	292	23.62	-10.32	245	25.26	-11.46	198	27.87	-11.89
338	22.38	-10.91	291	23.65	-10.27	244	25.29	-12.00	197	27.95	-11.47
337	22.41	-11.44	290	23.67	-10.03	243	25.33	-11.08	196	28.04	-11.19
336	22.44	-11.18	289	23.70	-9.59	242	25.37	-12.14	195	28.10	-11.83
335	22.46	-11.04	288	23.73	-9.41	241	25.41	-11.39	194	28.15	-12.36
334	22.49	-11.30	287	23.75	-9.65	240	25.45	-11.69	193	28.21	-12.69
333	22.52	-10.79	286	23.78	-10.13	239	25.49	-12.28	192	28.26	-11.81
332	22.54	-11.58	285	23.81	-10.39	238	25.53	-12.22	191	28.31	-11.51
331	22.57	-11.41	284	23.83	-10.30	237	25.57	-12.14	190	28.36	-11.27
330	22.60	-10.89	283	23.86	-10.78	236	25.61	-11.50	189	28.41	-10.97
329	22.62	-10.91	282	23.89	-9.91	235	25.65	-11.65	188	28.47	-11.85
328	22.65	-10.63	281	23.92	-9.46	234	25.69	-11.68	187	28.52	-11.17
327	22.68	-11.39	280	23.94	-9.07	233	25.72	-11.31	186	28.57	-11.66
326	22.71	-11.39	279	23.97	-9.21	232	25.76	-11.48	185	28.62	-11.93
325	22.73	-11.87	278	24.00	-10.55	231	25.80	-11.46	184	28.67	-11.26
324	22.76	-11.51	277	24.02	-9.45	230	25.84	-11.93	183	28.72	-11.23
323	22.79	-11.53	276	24.05	-10.77	229	25.88	-12.32	183	28.72	-11.08
322	22.81	-11.13	275	24.08	-11.24	228	25.92	-11.84	182	28.78	-12.04
321	22.84	-10.63	274	24.12	-10.69	227	25.96	-11.52	181	28.83	-11.34
320	22.87	-11.23	273	24.16	-10.08	226	26.00	-12.09	180	28.88	-10.95
319	22.89	-11.39	272	24.20	-9.67	225	26.04	-11.64	179	28.93	-11.56
318	22.92	-11.39	271	24.24	-8.95	224	26.08	-11.63	178	28.98	-11.52
317	22.95	-11.61	270	24.28	-10.15	223	26.12	-11.37	177	29.04	-10.92

Continue to next page

Supplementary Table S2 (Cont.)

Distance (mm)	Age (ky, BP)	$\delta^{18}\text{O}$ (‰, VPDB)									
176	29.09	-11.68	140	34.47	-10.31	104	37.46	-11.98	68	38.38	-10.19
175	29.14	-11.62	139	34.57	-9.87	103	37.48	-11.98	67	38.54	-10.45
174	29.19	-12.85	138	34.67	-10.58	102	37.50	-13.44	66	38.70	-11.96
173	29.43	-10.44	137	34.77	-10.94	101	37.52	-11.89	65	38.86	-10.02
172	29.86	-10.96	136	34.88	-11.50	100	37.54	-13.50	64	39.02	-10.20
171	30.30	-10.76	135	34.98	-11.17	99	37.56	-11.69	63	39.17	-10.53
170	30.73	-11.15	134	35.08	-11.11	98	37.58	-12.49	62	39.33	-11.37
169	31.16	-11.20	133	35.18	-11.50	97	37.60	-12.51	61	39.49	-10.43
168	31.59	-10.72	132	35.29	-10.70	96	37.62	-12.21	60	39.65	-10.03
167	31.69	-11.25	131	35.39	-10.64	95	37.64	-12.84	59	39.81	-9.94
166	31.79	-10.57	130	35.49	-10.80	94	37.66	-11.14	58	39.97	-11.06
165	31.90	-11.09	129	35.60	-10.62	93	37.68	-12.79	57	40.13	-11.86
164	32.00	-11.18	128	35.70	-11.80	92	37.70	-12.14	56	40.29	-11.67
163	32.10	-10.38	127	35.80	-12.34	91	37.72	-12.46	55	40.45	-10.96
162	32.20	-10.69	126	35.90	-12.25	90	37.74	-12.60	54	40.61	-11.16
161	32.31	-11.09	125	36.01	-12.56	89	37.76	-12.73	53	40.76	-11.40
160	32.41	-9.91	124	36.11	-12.12	88	37.78	-12.84	52	40.92	-13.45
159	32.51	-10.57	123	36.21	-10.65	87	37.80	-11.29	51	41.08	-11.99
158	32.62	-10.18	122	36.31	-11.29	86	37.81	-12.81	50	41.24	-12.26
157	32.72	-10.29	121	36.42	-11.34	85	37.83	-11.09	49	41.40	-10.13
156	32.82	-10.35	120	36.52	-11.06	84	37.85	-12.04	48	41.56	-10.68
155	32.92	-11.69	119	36.62	-9.88	83	37.87	-12.51	47	41.72	-11.39
154	33.03	-11.48	118	36.73	-11.13	82	37.89	-12.76	46	41.88	-11.77
153	33.13	-10.17	117	36.83	-11.63	81	37.91	-12.51	45	42.04	-11.82
152	33.23	-10.94	116	36.93	-12.16	80	37.93	-11.97	44	42.20	-11.62
151	33.34	-10.91	115	37.03	-11.68	79	37.95	-12.75	43	42.35	-12.52
150	33.44	-10.08	114	37.14	-13.08	78	37.97	-10.99	42	42.51	-11.99
149	33.54	-9.98	113	37.24	-11.95	77	37.99	-11.78	41	42.67	-12.60
148	33.64	-11.41	112	37.30	-11.20	76	38.01	-11.01	40	42.83	-11.12
147	33.75	-10.65	111	37.32	-12.74	75	38.03	-11.33	39	42.99	-11.43
146	33.85	-10.62	110	37.34	-13.96	74	38.05	-12.50	38	43.15	-13.33
145	33.95	-10.65	109	37.36	-12.78	73	38.07	-11.39	37	43.31	-11.43
144	34.05	-10.54	108	37.38	-12.66	72	38.09	-12.86	36	43.47	-11.08
143	34.16	-10.52	107	37.40	-13.90	71	38.11	-12.40	35	43.63	-11.95
142	34.26	-10.58	106	37.42	-13.85	70	38.13	-12.08			
141	34.36	-10.89	105	37.44	-11.89	69	38.22	-11.96			
<b>XBL-3</b>											
1	41.42	-10.87	11	40.43	-10.44	21	39.45	-9.24	33	38.46	-9.78
2	41.32	-10.83	12	40.33	-10.22	22	39.37	-8.29	35	38.29	-10.36
3	41.22	-10.95	13	40.23	-10.38	23	39.29	-8.51	37	38.13	-10.48
4	41.12	-10.92	14	40.13	-10.85	24	39.2	-8.81	39	37.93	-11.42
5	41.02	-10.29	15	40.03	-10.81	25	39.12	-9.11	41	37.69	-11.53
6	40.92	-10.68	16	39.93	-10.19	26	39.04	-9.07	43	37.46	-11.92
7	40.82	-10.25	17	39.83	-10.28	27	38.96	-8.91	45	37.22	-11.89
8	40.73	-10.23	18	39.73	-9.96	28	38.87	-8.86	47	36.98	-11.66
9	40.63	-9.93	19	39.63	-9.74	29	38.79	-8.75	49	36.75	-11.69
10	40.53	-10.17	20	39.53	-9.47	31	38.63	-9.34	51	36.51	-11.53

Continue to next page

Supplementary Table S2 (Cont.)

Distance (mm)	Age (ky, BP)	$\delta^{18}\text{O}$ (‰, VPDB)									
53	36.27	-11.59	112	34.87	-11.29	172	33.54	-11.08	232	32.47	-12.47
55	36.04	-11.48	114	34.82	-11.01	174	33.51	-11.36	234	32.39	-11.31
57	36	-11.22	116	34.76	-11.25	176	33.49	-11.35	236	32.32	-11.92
58	35.99	-11.37	118	34.71	-11.34	178	33.48	-11.76	238	32.25	-11.13
60	35.95	-11.41	120	34.65	-11.51	180	33.46	-11.85	240	32.17	-11.28
62	35.91	-11.18	122	34.6	-10.85	182	33.44	-10.54	242	32.1	-11.67
64	35.88	-10.65	124	34.55	-11.08	184	33.43	-11.24	244	32.03	-11.53
66	35.84	-10.76	126	34.49	-11.01	186	33.41	-11.53	246	31.96	-11.06
68	35.81	-10.59	128	34.44	-11.55	188	33.39	-11.05	248	31.88	-11.78
70	35.77	-10.38	130	34.38	-11.12	190	33.38	-10.54	250	31.81	-11.26
72	35.74	-10.19	132	34.33	-11.39	192	33.36	-10.96	252	31.74	-12.13
74	35.7	-10.27	134	34.28	-11.38	194	33.34	-10.58	254	31.65	-11.49
76	35.67	-9.51	136	34.24	-10.9	196	33.33	-10.82	256	31.55	-11.05
78	35.63	-10.7	138	34.2	-10.74	198	33.31	-10.61	258	31.44	-11.49
80	35.6	-10.35	140	34.16	-11.47	200	33.29	-10.82	260	31.34	-11.79
82	35.56	-10.35	142	34.13	-10.38	202	33.28	-10.7	262	31.23	-11.42
84	35.53	-10.95	144	34.09	-10.76	204	33.26	-10.6	264	31.13	-11.13
86	35.49	-11.13	146	34.05	-11.91	206	33.24	-10.78	266	31.03	-11.91
88	35.46	-11.01	148	34.01	-11.67	208	33.23	-11	268	30.92	-11.41
90	35.42	-11.88	150	33.97	-11.5	210	33.21	-10.76	270	30.82	-12.3
92	35.39	-10.82	152	33.93	-10.98	212	33.19	-10.76	272	30.72	-11.84
94	35.35	-12	154	33.89	-11.7	214	33.12	-12.16	274	30.61	-11.4
96	35.31	-11.12	156	33.85	-12.4	216	33.05	-12.47	276	30.51	-11.85
98	35.25	-11.57	158	33.81	-11.35	218	32.98	-11.85	278	30.4	-11.22
100	35.2	-11.72	160	33.77	-11.71	220	32.9	-11.73	280	30.3	-10.09
102	35.14	-12.16	162	33.73	-11.6	222	32.83	-12.33	282	30.22	-10.57
104	35.09	-11.92	164	33.7	-11.45	224	32.76	-12.23	284	30.14	-10.97
106	35.03	-11.38	166	33.66	-11.7	226	32.68	-11.86			
108	34.98	-11	168	33.62	-11.72	228	32.61	-11.96			
110	34.93	-11.39	170	33.58	-11.23	230	32.54	-11.45			
<b>XBL-7</b>											
2	71.00	-10.68	34	70.11	-10.08	66	67.48	-9.07	98	64.68	-11.74
4	70.94	-10.20	36	70.05	-10.31	68	67.31	-9.38	100	64.50	-11.05
6	70.89	-9.91	38	69.94	-9.20	70	67.13	-9.49	102	64.36	-10.33
8	70.83	-10.31	40	69.76	-9.45	72	66.96	-9.46	104	64.22	-12.83
10	70.77	-10.08	42	69.59	-10.11	74	66.78	-9.42	106	64.07	-11.23
12	70.72	-9.35	44	69.41	-10.04	76	66.61	-8.86	108	63.91	-11.07
14	70.66	-10.09	46	69.23	-9.82	78	66.43	-9.56	110	63.75	-11.12
16	70.61	-9.76	48	69.06	-10.51	80	66.25	-10.62	112	63.59	-10.16
18	70.55	-9.64	50	68.88	-10.66	82	66.08	-10.75	114	63.43	-10.55
20	70.50	-10.59	52	68.71	-10.16	84	65.90	-10.67	116	63.27	-10.90
22	70.44	-10.30	54	68.53	-9.70	86	65.73	-11.00	118	63.11	-10.53
24	70.39	-9.91	56	68.36	-9.85	88	65.55	-11.01	120	62.95	-10.82
26	70.33	-10.73	58	68.18	-10.00	90	65.38	-10.60	122	62.79	-9.92
28	70.27	-9.92	60	68.01	-10.42	92	65.20	-10.91	124	62.63	-10.17
30	70.22	-10.37	62	67.83	-9.97	94	65.03	-11.39	126	62.47	-10.07
32	70.16	-10.03	64	67.66	-9.28	96	64.85	-11.03	128	62.31	-9.68

Continue to next page

Supplementary Table S2 (Cont.)

Distance (mm)	Age (ky, BP)	$\delta^{18}\text{O}$ (‰, VPDB)									
130	62.15	-10.15	160	61.32	-10.24	188	60.97	-11.96	216	60.27	-11.27
132	61.99	-8.82	162	61.30	-10.45	190	60.92	-11.01	218	60.22	-11.47
134	61.83	-11.51	164	61.27	-10.39	192	60.87	-10.65	220	60.17	-11.70
136	61.67	-10.71	166	61.25	-10.42	194	60.82	-11.42	222	60.12	-11.73
138	61.58	-11.00	168	61.23	-10.62	196	60.77	-11.37	224	60.07	-12.00
140	61.55	-10.25	170	61.20	-10.75	198	60.72	-11.07	226	60.02	-11.68
142	61.53	-10.79	172	61.18	-10.43	200	60.67	-10.74	228	59.97	-10.37
144	61.51	-10.48	174	61.16	-10.94	202	60.62	-10.69	230	59.92	-10.14
146	61.48	-10.04	176	61.13	-11.38	204	60.57	-11.48	232	59.87	-10.27
148	61.46	-9.50	178	61.11	-11.16	206	60.52	-11.75	234	59.82	-11.50
150	61.44	-10.12	180	61.09	-10.97	208	60.47	-11.56	236	59.77	-11.26
154	61.39	-10.20	182	61.06	-10.77	210	60.42	-11.42	238	59.72	-11.14
156	61.37	-10.28	184	61.04	-11.46	212	60.37	-11.52	240	59.67	-11.30
158	61.34	-10.65	186	61.02	-11.13	214	60.32	-10.78			
<b>XBL-4</b>											
2	81.951	-13.73	50	81.882	-14.40	114	81.790	-13.59	168	81.081	-12.94
4	81.948	-14.23	52	81.879	-14.58	116	81.787	-14.00	170	81.010	-13.32
6	81.945	-14.18	54	81.876	-15.01	118	81.784	-13.60	172	80.939	-13.93
7	81.943	-14.09	56	81.873	-14.88	120	81.781	-13.32	171	80.974	-13.46
8	81.942	-13.22	58	81.870	-14.33	122	81.778	-13.83	174	80.868	-13.11
10	81.939	-13.27	60	81.867	-14.18	124	81.776	-13.96	176	80.796	-13.52
12	81.936	-13.46	62	81.865	-14.31	125	81.774	-13.38	177	80.761	-13.43
14	81.933	-13.64	64	81.862	-14.19	126	81.773	-13.66	178	80.725	-12.99
16	81.930	-14.25	66	81.859	-14.10	127	81.771	-13.71	180	80.654	-13.38
18	81.928	-14.27	68	81.856	-14.39	128	81.770	-13.84	182	80.583	-13.98
20	81.925	-13.81	70	81.853	-13.92	130	81.767	-13.47	184	80.512	-13.73
22	81.922	-13.59	72	81.850	-14.04	132	81.764	-13.73	186	80.441	-14.30
24	81.919	-14.01	74	81.847	-14.08	132	81.764	-13.97	187	80.405	-13.79
26	81.916	-13.99	76	81.844	-14.14	134	81.761	-14.11	188	80.370	-13.44
27	81.915	-13.87	78	81.842	-13.86	136	81.758	-13.84	190	80.298	-14.16
28	81.913	-13.46	80	81.839	-13.93	138	81.755	-13.43	192	80.227	-13.56
29	81.912	-14.37	82	81.836	-14.50	140	81.753	-13.48	194	80.156	-13.36
30	81.910	-14.18	84	81.833	-13.55	142	81.750	-13.41	196	80.085	-13.49
31	81.909	-14.01	86	81.830	-13.31	144	81.747	-13.55	198	80.014	-12.92
32	81.908	-13.27	88	81.827	-13.90	146	81.744	-13.74	200	79.943	-13.23
34	81.905	-13.68	90	81.824	-13.99	148	81.741	-14.18	202	79.872	-13.23
36	81.902	-13.89	92	81.821	-14.46	150	81.721	-14.51	204	79.773	-12.82
38	81.899	-13.79	94	81.819	-14.22	152	81.650	-13.98	206	79.648	-12.89
40	81.896	-14.25	96	81.816	-14.01	154	81.579	-13.18	208	79.523	-12.53
41	81.895	-14.08	98	81.813	-13.74	156	81.508	-14.10	209	79.460	-13.07
42	81.893	-13.61	100	81.810	-13.69	157	81.472	-13.67	210	79.398	-13.55
43	81.892	-14.13	102	81.807	-13.79	158	81.437	-14.15	211	79.335	-12.75
44	81.890	-14.37	104	81.804	-14.00	160	81.366	-14.36	212	79.272	-12.49
45	81.889	-14.68	106	81.801	-14.10	162	81.294	-13.37	214	79.147	-12.35
46	81.887	-13.73	108	81.799	-13.91	163	81.259	-13.93	216	79.022	-12.90
47	81.886	-13.71	110	81.796	-14.30	164	81.223	-13.73	218	78.897	-12.73
48	81.885	-14.69	112	81.793	-14.02	166	81.152	-13.40	220	78.771	-12.78

Continue to next page

Supplementary Table S2 (Cont.)

Distance (mm)	Age (ky, BP)	$\delta^{18}\text{O}$ (‰, VPDB)									
222	78.646	-13.06	236	77.769	-12.68	250	75.602	-11.95	264	73.069	-10.50
224	78.521	-13.06	238	77.501	-12.99	252	75.285	-10.80	266	72.116	-10.30
226	78.396	-12.93	240	77.184	-12.95	254	74.969	-10.80	268	71.164	-10.17
228	78.270	-12.01	242	76.868	-12.37	256	74.653	-11.08	270	70.211	-9.65
230	78.145	-12.93	244	76.551	-12.60	258	74.336	-11.12	272	60.103	-9.22
232	78.020	-13.19	246	76.235	-13.00	260	74.020	-11.37	274	58.761	-9.40
234	77.895	-12.97	248	75.918	-12.68	262	73.703	-11.06	276	57.418	-10.31
<b>XBL-48</b>											
13	106.54	-15.74	48	104.85	-11.55	83	93.12	-10.48	146	85.46	-9.76
14	106.49	-15.19	49	104.79	-11.75	84	92.44	-9.88	148	85.16	-9.67
15	106.45	-15.14	50	104.74	-11.60	85	91.75	-10.20	150	84.86	-9.63
16	106.40	-15.00	51	104.68	-11.44	86	91.07	-9.96	152	84.56	-9.49
17	106.36	-15.23	52	104.62	-12.20	87	90.71	-10.29	154	84.27	-9.88
18	106.32	-15.04	53	104.57	-11.37	88	90.69	-9.74	156	83.97	-9.78
19	106.27	-14.64	54	104.51	-11.92	89	90.67	-9.84	158	83.67	-10.29
20	106.23	-15.24	55	104.46	-11.54	90	90.64	-10.34	160	83.37	-9.82
21	106.19	-15.27	56	104.40	-10.93	92	90.60	-10.45	161	83.22	-9.76
22	106.14	-14.59	57	104.35	-10.80	94	90.55	-10.70	162	83.08	-9.58
23	106.10	-14.61	58	104.29	-11.90	96	90.50	-10.60	163	82.93	-9.67
24	106.06	-15.32	59	104.24	-11.09	98	90.46	-10.79	164	82.78	-9.93
25	106.01	-15.40	60	104.18	-11.78	100	90.41	-10.43	165	82.63	-9.51
26	105.97	-15.08	61	104.13	-11.79	102	90.27	-10.33	166	82.47	-12.82
27	105.93	-15.14	62	104.07	-11.90	104	89.87	-11.85	167	82.30	-12.16
28	105.88	-15.55	63	104.02	-11.64	106	89.47	-11.89	168	82.14	-14.57
29	105.84	-15.30	64	103.96	-11.29	108	89.15	-11.80	169	81.98	-13.11
30	105.80	-14.73	65	103.90	-12.21	110	89.07	-11.87	170	81.82	-12.93
31	105.75	-15.69	66	102.83	-14.13	112	88.99	-12.14	171	81.65	-14.07
32	105.71	-15.12	67	102.57	-14.69	114	88.91	-11.41	172	81.49	-13.11
33	105.67	-15.48	68	102.20	-14.41	116	88.83	-12.27	174	81.17	-13.39
34	105.62	-15.70	69	101.83	-13.54	118	88.75	-11.85	176	80.84	-13.36
35	105.57	-15.07	70	101.47	-14.00	120	88.67	-10.84	178	80.51	-12.75
36	105.51	-15.12	71	101.10	-13.73	122	88.59	-11.74	180	80.19	-13.32
37	105.46	-14.55	72	100.73	-13.26	124	88.51	-10.27	182	79.86	-13.11
38	105.40	-13.96	73	100.37	-14.25	126	88.43	-9.68	184	79.54	-12.44
39	105.34	-14.93	74	99.63	-12.65	128	88.13	-10.30	186	79.21	-11.71
40	105.29	-15.06	75	98.90	-12.18	130	87.83	-9.54	188	78.89	-12.59
41	105.23	-14.93	76	98.16	-11.90	132	87.54	-9.52	190	78.56	-12.31
42	105.18	-14.55	77	97.43	-12.19	134	87.24	-9.96	192	78.24	-12.26
43	105.12	-12.58	78	96.69	-11.85	136	86.94	-9.98	194	77.91	-12.61
44	105.07	-12.11	79	95.96	-11.00	138	86.64	-10.35	196	77.59	-12.62
45	105.01	-10.98	80	95.22	-10.77	140	86.35	-10.32	198	77.26	-12.22
46	104.96	-12.31	81	94.49	-10.84	142	86.05	-10.46	200	76.94	-12.39
47	104.90	-11.78	82	93.80	-10.64	144	85.75	-10.44	202	76.61	-11.11
<b>XBL-65</b>											
35	170.73	-14.15	38	170.66	-15.17	44	170.52	-13.78	48	170.42	-14.31
36	170.71	-14.55	40	170.62	-14.81	45	170.50	-14.51	50	170.38	-14.60
37	170.69	-14.56	42	170.57	-14.43	46	170.47	-13.57	52	170.33	-14.17

Continue to next page

Supplementary Table S2 (Cont.)

Distance (mm)	Age (ky, BP)	$\delta^{18}\text{O}$ (‰, VPDB)									
54	170.28	-14.57	108	169.84	-13.92	160	168.76	-12.65	212	168.61	-11.52
55	170.26	-13.70	110	169.79	-13.25	162	168.75	-11.97	214	168.61	-12.34
56	170.23	-13.24	112	169.73	-13.49	164	168.75	-13.31	215	168.59	-12.38
58	170.18	-14.22	114	169.68	-13.95	165	168.74	-11.59	216	168.56	-11.41
60	170.14	-14.37	115	169.65	-14.14	166	168.74	-11.70	218	168.51	-11.27
65	170.02	-12.89	116	169.62	-13.44	168	168.74	-11.77	220	168.45	-11.61
66	170.00	-13.61	118	169.57	-13.96	170	168.73	-11.76	222	168.40	-11.33
68	170.00	-13.80	120	169.51	-14.02	172	168.73	-11.94	224	168.34	-11.92
70	170.00	-14.26	122	169.46	-14.63	174	168.72	-12.54	225	168.32	-11.34
72	170.00	-12.94	124	169.41	-14.51	175	168.72	-12.11	226	168.29	-11.59
74	170.00	-14.75	125	169.38	-13.69	176	168.71	-11.67	228	168.23	-11.99
75	169.99	-14.09	126	169.35	-13.27	178	168.71	-11.12	230	168.18	-11.74
76	169.99	-13.81	128	169.30	-13.79	180	168.70	-11.94	232	168.12	-12.11
78	169.99	-14.49	130	169.24	-13.42	182	168.70	-11.05	234	168.07	-12.04
80	169.99	-13.62	132	169.19	-13.00	184	168.69	-12.05	235	168.04	-12.07
82	169.99	-14.63	134	169.14	-13.49	185	168.69	-12.00	236	168.02	-11.54
84	169.98	-13.32	135	169.11	-13.87	186	168.69	-11.43	238	167.96	-12.76
85	169.98	-13.82	136	169.08	-13.76	188	168.68	-12.00	240	167.91	-12.57
86	169.98	-13.70	138	169.03	-13.46	190	168.67	-12.21	242	167.85	-12.27
88	169.98	-13.65	140	168.97	-14.03	192	168.67	-11.81	244	167.80	-12.37
90	169.98	-13.84	142	168.92	-13.80	194	168.66	-11.42	245	167.74	-12.44
92	169.97	-13.58	144	168.87	-13.00	195	168.66	-11.27	246	167.69	-11.94
94	169.97	-13.51	145	168.84	-13.55	196	168.66	-12.34	248	167.63	-12.42
95	169.97	-13.81	146	168.81	-13.64	198	168.65	-12.12	250	167.58	-11.62
96	169.97	-13.69	148	168.79	-14.13	200	168.65	-11.81	252	167.52	-12.30
98	169.97	-13.39	150	168.79	-14.50	202	168.64	-12.59	254	167.47	-11.90
100	169.97	-13.85	152	168.78	-13.11	204	168.63	-12.15	255	167.41	-11.45
102	169.96	-13.78	154	168.78	-13.02	205	168.63	-12.23	256	167.36	-12.12
104	169.95	-13.31	155	168.77	-11.88	206	168.63	-12.71	258	167.30	-11.04
105	169.92	-13.75	156	168.77	-12.27	208	168.62	-12.67	260	167.25	-9.74
106	169.89	-13.37	158	168.76	-11.36	210	168.62	-11.45			
<b>XBL-27</b>											
4	189.46	-9.87	64	185.19	-10.34	124	183.98	-10.28	184	180.79	-11.02
8	189.06	-10.35	68	185.11	-10.23	128	183.79	-9.99	188	180.53	-10.68
12	188.66	-9.30	72	185.04	-9.85	132	183.6	-10.30	192	180.26	-13.43
16	188.26	-10.71	76	184.97	-9.80	136	183.4	-9.71	196	180	-14.04
20	187.87	-10.41	80	184.89	-10.36	140	183.21	-9.80	200	179.74	-14.25
24	187.47	-10.09	84	184.82	-10.25	144	183.02	-10.28	202	179.6	-13.76
28	187.07	-9.75	88	184.74	-10.10	148	182.82	-10.19	204	179.47	-12.85
32	186.68	-9.79	92	184.67	-9.84	152	182.63	-9.36	208	179.21	-12.84
36	186.28	-9.86	96	184.59	-9.71	156	182.44	-11.12	212	178.95	-12.91
40	185.88	-9.90	100	184.52	-10.31	160	182.25	-11.14	216	178.78	-13.56
44	185.56	-10.55	104	184.44	-10.32	164	182.05	-10.61	220	178.63	-13.33
48	185.49	-9.75	108	184.37	-9.13	168	181.84	-10.97	224	178.49	-12.76
52	185.41	-10.16	112	184.29	-10.07	172	181.58	-9.65	228	178.35	-13.07
56	185.34	-10.29	116	184.22	-9.77	176	181.32	-9.50	232	178.21	-12.63
60	185.26	-10.33	120	184.14	-9.60	180	181.05	-9.11	236	178.07	-12.60

Continue to next page

Supplementary Table S2 (Cont.)

Distance (mm)	Age (ky, BP)	$\delta^{18}\text{O}$ (‰, VPDB)									
240	177.92	-14.00	272	176.95	-13.42	304	176.73	-12.70	336	174.39	-13.95
244	177.78	-12.38	276	176.94	-13.34	308	176.44	-12.31	340	174.1	-13.70
248	177.64	-12.19	280	176.93	-12.61	312	176.14	-12.96	344	173.8	-13.96
252	177.5	-13.30	284	176.92	-13.34	316	175.85	-12.33	348	173.51	-14.71
256	177.35	-13.00	288	176.91	-13.20	320	175.56	-14.00	352	173.22	-13.56
260	177.21	-12.98	292	176.9	-14.54	324	175.27	-14.67	356	172.93	-13.78
264	177.07	-13.91	296	176.89	-12.55	328	174.97	-13.81	360	172.63	-14.99
268	176.96	-13.45	300	176.88	-11.98	332	174.68	-13.58	364	172.34	-13.23
<b>XBL-26</b>											
2	251.96	-11.53	78	240.63	-11.75	154	223.32	-11.32	230	201.59	-10.33
4	251.79	-12.82	80	240.36	-14.15	156	223.22	-11.35	232	201.56	-9.41
6	251.61	-11.62	82	240.09	-13.73	158	223.11	-11.04	234	201.53	-9.28
8	251.43	-10.38	84	239.88	-13.84	160	223.01	-12.65	236	201.50	-9.12
10	251.26	-12.83	86	239.67	-14.50	162	222.90	-13.31	238	201.47	-9.78
12	251.08	-12.14	88	239.46	-12.48	164	222.80	-12.46	240	201.45	-9.11
14	250.91	-12.10	90	239.25	-13.27	166	222.69	-11.94	242	201.42	-9.39
16	250.73	-11.63	92	239.04	-13.60	168	222.59	-11.80	244	201.39	-8.87
18	250.55	-11.76	94	238.83	-13.13	170	222.48	-11.71	246	201.36	-9.28
20	250.38	-12.13	96	238.62	-12.72	172	222.38	-11.83	248	201.34	-9.62
22	250.20	-12.54	98	238.41	-12.97	174	217.17	-11.68	250	201.31	-9.32
24	250.03	-11.98	100	238.20	-13.29	176	216.81	-12.19	252.7	201.23	-8.69
26	249.85	-12.15	102	237.99	-13.00	178	216.46	-11.21	253.4	201.20	-8.91
28	249.67	-11.64	104	237.78	-12.77	180	216.10	-11.87	254	201.17	-9.03
30	249.50	-10.67	106	237.57	-13.67	182	215.74	-11.82	254.7	201.14	-8.99
32	249.32	-10.03	108	237.36	-12.43	184	215.38	-10.73	255.4	201.11	-9.17
34	249.15	-10.84	110	237.15	-12.89	186	215.02	-11.50	256	201.08	-8.79
36	248.97	-10.49	112	236.94	-12.62	188	214.66	-11.21	256.7	201.05	-9.04
38	248.79	-10.30	114	236.73	-12.89	190	214.30	-12.51	257.4	201.02	-9.39
40	248.49	-9.85	116	236.52	-12.81	192	204.41	-9.82	258	201.00	-8.99
42	248.06	-9.85	118	236.31	-13.23	194	204.14	-9.41	258.7	200.96	-8.72
44	247.63	-10.36	120	236.10	-13.68	196	203.87	-9.48	259.4	200.93	-8.93
46	247.20	-10.18	122	235.89	-12.90	198	203.60	-8.81	260	200.91	-8.82
48	246.77	-9.85	124	235.68	-12.79	200	203.33	-9.29	260.7	200.88	-8.61
50	246.34	-9.76	126	234.45	-12.81	202	203.06	-9.02	261.4	200.85	-8.15
52	245.91	-10.05	128	232.20	-9.51	204	202.79	-9.60	262	200.82	-8.70
54	245.48	-9.81	130	229.95	-10.09	206	202.52	-9.67	262.7	199.97	-8.57
56	245.05	-9.41	132	227.69	-10.76	208	202.26	-9.95	263.4	199.12	-15.87
58	244.62	-8.96	134	225.44	-10.87	210	201.99	-10.53	264	198.39	-15.77
60	244.19	-9.67	136	224.26	-10.25	212	201.84	-9.84	264.7	197.54	-14.74
62	243.76	-9.54	138	224.16	-11.57	214	201.81	-10.26	265.4	196.69	-14.20
64	243.33	-8.85	140	224.05	-11.51	216	201.78	-10.17	266	195.96	-14.95
66	242.90	-8.70	142	223.95	-10.52	218	201.75	-10.06	266.7	195.11	-15.70
68	242.47	-8.57	144	223.85	-10.78	220	201.73	-10.12	267.4	194.26	-14.23
70	242.04	-7.89	146	223.74	-10.65	222	201.70	-10.21	268	193.53	-15.86
72	241.61	-8.99	148	223.64	-11.44	224	201.67	-9.36	268.7	192.68	-15.64
74	241.18	-9.43	150	223.53	-11.43	226	201.64	-9.60	269.4	191.82	-15.85
76	240.90	-8.66	152	223.43	-11.09	228	201.61	-10.06	270	191.10	-16.01

Continue to next page

Supplementary Table S2 (Cont.)

Distance (mm)	Age (ky, BP)	$\delta^{18}\text{O}$ (‰, VPDB)									
270.7	190.24	-15.43	304	186.61	-10.20	398	180.33	-9.59	475.5	160.34	-10.74
271.4	189.39	-12.80	306	186.49	-10.89	400	180.19	-9.88	476	160.00	-10.5
272	188.66	-9.83	308	186.36	-11.13	402	180.04	-10.54	476.5	159.66	-10.74
272.7	188.62	-9.70	310	186.23	-10.25	404	179.90	-9.69	477	159.31	-10.43
273.4	188.57	-10.06	312	186.10	-10.43	406	179.75	-9.34	477.5	158.97	-10.66
274	188.54	-10.02	314	185.97	-10.48	408	175.36	-13.38	478	158.63	-10.33
274.7	188.49	-9.93	316	185.84	-10.72	410	175.22	-12.86	478.5	158.29	-10.58
275.4	188.45	-9.71	318	185.72	-11.38	412	175.08	-12.22	479	157.95	-10.53
276	188.41	-9.27	320	185.59	-10.78	414	174.93	-13.10	479.5	157.60	-10.62
276.7	188.36	-9.24	322	185.46	-9.73	416	174.79	-11.74	480	157.26	-9.84
277.4	188.32	-10.29	324	185.33	-10.16	418	174.64	-11.94	480.5	156.92	-10.03
278	188.28	-11.39	326	185.20	-10.57	420	174.50	-12.66	481	156.58	-9.87
278.7	188.23	-10.85	328	185.08	-10.53	422	174.36	-12.41	481.5	156.23	-9.9
279.4	188.19	-11.61	330	184.95	-10.15	424	174.21	-13.01	482	155.89	-9.71
280	188.15	-11.12	332	184.82	-10.27	426	174.07	-11.82	482.5	155.55	-9.88
280.7	188.11	-10.96	334	184.69	-11.55	428	173.93	-12.30	483	155.21	-10.68
281.4	188.06	-11.05	336	184.56	-11.92	430	173.78	-12.74	483.5	154.86	-10.42
282	188.02	-11.32	338	184.43	-11.18	431	173.71	-12.86	484	154.52	-10.15
282.7	187.98	-11.03	340	184.31	-10.70	432	173.64	-15.48	484.5	154.18	-10.63
283.4	187.93	-11.68	342	184.18	-10.85	433	173.57	-13.26	485	153.84	-11.01
284	187.90	-10.97	344	184.05	-10.32	434	173.49	-13.18	485.5	153.49	-10.2
284.7	187.85	-11.61	346	183.92	-10.85	436	173.35	-12.93	486	153.15	-9.82
285.4	187.81	-11.45	348	183.79	-10.14	438	173.21	-14.30	486.5	152.81	-10.74
286	187.77	-10.93	350	183.67	-11.40	440	173.06	-13.03	487	152.47	-11.09
286.7	187.72	-11.28	352	183.54	-10.46	442	172.92	-13.00	487.5	152.13	-11.15
287.4	187.68	-10.66	354	183.41	-11.13	444	172.77	-13.79	488	151.78	-10.95
288	187.64	-10.97	356	183.28	-10.87	446	172.63	-14.27	488.5	151.44	-10.42
288.7	187.59	-10.22	358	183.15	-11.75	448	172.49	-14.59	489	151.10	-10.86
289.4	187.55	-11.10	360	183.02	-11.27	450	172.34	-15.79	489.5	150.76	-11.58
290	187.51	-11.28	362	182.90	-9.42	452	172.20	-14.20	490	150.41	-11.2
290.7	187.47	-10.67	364	182.77	-10.27	454	172.06	-13.62	490.5	150.07	-11.29
291.4	187.42	-11.47	366	182.64	-9.63	456	171.91	-13.96	491	149.73	-11.83
292	187.38	-10.59	368	182.50	-10.08	458	171.77	-13.97	491.5	149.39	-11.45
292.7	187.34	-10.82	370	182.35	-11.03	460	171.62	-14.82	492	149.04	-11.08
293.4	187.29	-10.42	372	182.21	-9.32	462	171.48	-14.49	492.5	148.70	-10.92
294	187.25	-10.58	374	182.06	-11.43	464	171.34	-14.90	493	148.36	-10.29
294.7	187.21	-9.82	376	181.92	-10.56	466	171.19	-15.02	493.5	148.02	-10.56
295.4	187.16	-10.64	378	181.77	-10.27	468	171.05	-16.04	494	147.67	-10.39
296	187.13	-10.56	380	181.63	-9.37	470	164.11	-10.14	494.5	147.33	-10.85
296.7	187.08	-11.76	382	181.49	-10.66	471.5	163.08	-10.63	495	146.99	-10.91
297.4	187.04	-10.39	384	181.34	-9.79	472	162.74	-10.39	495.5	146.65	-10.88
298	187.00	-10.60	386	181.20	-10.24	472.5	162.40	-10.63	496	146.31	-10.57
298.7	186.95	-11.33	388	181.05	-10.09	473	162.05	-11.44	496.5	145.96	-10.58
299.4	186.91	-10.64	390	180.91	-10.53	473.5	161.71	-10.77	497	145.62	-9.56
300	186.87	-9.98	392	180.76	-10.08	474	161.37	-10.39	497.5	145.28	-10.41
300.7	186.83	-9.45	394	180.62	-9.91	474.5	161.03	-11.01	498	144.94	-10.61
302	186.74	-9.34	396	180.48	-10.32	475	160.68	-10.46	498.5	144.59	-10.57

Continue to next page

Supplementary Table S2 (Cont.)

Distance (mm)	Age (ky, BP)	$\delta^{18}\text{O}$ (‰, VPDB)									
499	144.25	-10.7	508.5	136.84	-10.86	518	128.41	-14	527.5	108.50	-15.98
499.5	143.91	-10.56	509	136.39	-11	518.5	127.97	-15.78	528	106.42	-17.21
500	143.57	-11.43	509.5	135.95	-10.18	519	127.53	-14.85	528.5	104.33	-16.7
500.5	143.22	-11.24	510	135.51	-10.39	519.5	127.08	-14.37	529	102.25	-15.14
501	142.88	-11.39	510.5	135.06	-9.94	520	126.64	-14.41	529.5	100.16	-14.53
501.5	142.54	-11.32	511	134.62	-10.21	520.5	126.20	-16.55	530	98.08	-13.85
502	142.20	-11.05	511.5	134.18	-10.76	521	125.75	-15.39	530.5	95.99	-11.37
502.5	141.85	-10.97	512	133.73	-10.25	521.5	125.31	-15.94	531	93.91	-11.32
503	141.51	-11.14	512.5	133.29	-10.64	522	124.87	-14.46	531.5	91.82	-9.78
503.5	141.17	-10.75	513	132.85	-10.31	522.5	124.42	-17.27	532	89.74	-10.21
504	140.83	-10.59	513.5	132.40	-10.37	523	123.98	-17.78	532.5	87.65	-12.82
504.5	140.38	-10.98	514	131.96	-10.35	523.5	123.54	-16.2	533	85.57	-10.39
505	139.94	-10.49	514.5	131.52	-9.61	524	123.09	-16.17	533.5	83.49	-10.61
505.5	139.50	-11.14	515	131.07	-10.03	524.5	121.01	-14.38	534	81.40	-10.12
506	139.05	-10.99	515.5	130.63	-10.48	525	118.92	-14.24	534.5	79.32	-12.67
506.5	138.61	-11.05	516	130.19	-10.12	525.5	116.84	-14	535	77.23	-11.83
507	138.17	-10.43	516.5	129.74	-9.59	526	114.75	-14.73	535.5	75.15	-10.26
507.5	137.72	-10.67	517	129.30	-9.85	526.5	112.67	-16.47	536	73.06	-10.08
508	137.28	-10.3	517.5	128.86	-10.47	527	110.58	-14.86			